THE UNIVERSITY OF CALIFORNIA,

IRVINE

Analytical Tools to Probe Solid-Liquid Interfaces in Single Pores

DISSERTATION

Submitted in partial satisfaction of the requirements

for the degree of

DOCTOR OF PHILOSOPHY

In Chemistry

by

Wilfred S. Russell

Dissertation Committee:
Professor Zuzanna S. Siwy, Chair
Professor Ioan Andricioaei
Professor Allon I. Hochbaum

2022

DEDICATION

I dedicate this work to my parents, John H. Russell III, and Nona S. Russell for the constant love and support they have been bestowing upon me my whole life. I sincerely hope that I have repaid all the faith you have both put into me. As I have done in the past, I will always try to return your love and trust to the best of my abilities, and as long as I feel your support, I will never give up. This is for you. I thank you from the bottom of my heart. Peace.

TABLE OF CONTENTS

LIST OF FIGURES

ACKNOWLEDGEMENTS

I would like to acknowledge the GSI Helmholtzzentrum für Schwerionenforschung in Darmstadt, Germany and the Laser Spectroscopy Labs at the University of California, Irvine. Additionally, this work was supported as part of the Center for Enhanced Nanofluidic Transport, an Energy Frontier Research Center funded by the U.S. Department of Energy, Office of Science, Basic Energy Sciences at the University of California, Irvine under award # DE-SC0019112.

VITA

Wilfred S. Russell

EDUCATION

UNIVERSITY OF CALIFORNIA, IRVINE – Department of Chemistry, Irvine, CA, USA.
PhD Candidate: Chemistry (Analytical), September 2017 – June 2021. GPA: 3.975/4.0
UNIVERSITY OF ARIZONA – Department of Chemistry and Biochemistry (CBC), Tucson, AZ, USA.
Master of Science: Chemistry (Analytical), August 2014 – April 2017.
Bachelor of Science: Chemistry (ACS Certified), August 2009 – May 2014.
UNIVERSITY OF COPENHAGEN – Department of Chemistry, Copenhagen, Denmark.
Erasumus Exchange Student, August 2011 – June 2012.

WORK EXPERIENCE

UNIVERSITY OF CALIFORNIA, IRVINE – Department of Chemistry, Irvine, CA, USA.
Graduate Student Researcher (PhD Candidate) – May 2018 – June 2021.
MASSACHUSETTS INSTITUTE OF TECHNOLOGY – Center for Enhanced Nanofluidic Transport (CENT), The Department of Energy – Irvine, CA, USA.
Collaboratorative Research Scientist – October 2018 – June 2021.
UNIVERSITY OF ARIZONA – Department of Chemistry and Biochemistry, Tucson, AZ, USA.
Under/Graduate Student Researcher – August 2013 – April 2017.
UNIVERSITY OF ARIZONA – Departments of Pharmacology, Anesthesiology, Tucson, AZ, USA.
Collaboratorative Research Scientist – May 2015 – January 2016.
UNIVERSITY OF COPENHAGEN – Department of Chemistry, Copenhagen, Denmark.
Erasmus Exchange/Undergraduate Student Researcher – August 2011 – June 2012.

PUBLICATIONS

1. Vreeland, R. F., Atcherley, C. W., **Russell, W. S.,** Xie, J. Y., Lu, D., Laude, N. D., Porreca, F., & Heien, M. L. (2015). Biocompatible PEDOT: Nafion Composite Electrode Coatings for Selective Detection of Neurotransmitters in Vivo. Analytical Chemistry, 87 (5), 2600-2607.

2. **Russell, W. S.** PEDOT:Perchlorate coatings for the enhancement of biogenic amine detection at platinum. MS Dissertation, The University of Arizona, Tucson, AZ, USA, 2017.
3. **Russell, W. S.,** Siwy, Z. S. Enhanced Electroosmosis in Propylene Carbonate Salt Solutions. J. Chem. Phys., 154 (13), 1–9.
4. **Russell, W. S.,** Lin, C-Y., Siwy, Z. S. Gating of Ion Current with Charge Inversion. *Manuscript in preparation.*

ABSTRACT OF THE DISSERTATION

Analytical Tools to Probe Solid-Liquid Interfaces in Single Pores

by

Wilfred S. Russell

Doctor of Philosophy in Chemistry

University of California, Irvine, 2022

Professor Zuzanna S. Siwy, Thesis Chair

Meso- and nano- pores of well-defined geometries and surface charge characteristics are often employed as model systems to probe the electrochemical properties of solid-liquid interfaces. The high surface area to volume ratio and tunable surface charge of these porous systems gives them fascinating ion transport properties that dominate by controlling the solid-liquid interface. These unique transport properties also affect many processes such as the performance of membrane separation (desalination) systems. In this doctoral dissertation, we report experiments designed to facilitate the systematic studying of ionic transport and solid-liquid interfaces using single polyethylene terephthalate (PET) pores in two separate projects:

The first using cylindrical pores, ~ 1 μm in diameter (and 12 μm in length), and the resistive-pulse technique, to investigate the electroosmotic transport of unfunctionalized polystyrene particles through the PET pore in organic, propylene carbonate solutions of $LiClO_4$. The direction of electroosmotic particle translocation informs us about the surface potential of the pore walls and their duration, a measure of the particles' velocity and the pore walls' zeta potential. Our experiments show that the carboxlyated, as prepared surface of PET pore(s) become positively charged in $LiClO_4$ solutions of propylene carbonate, even though in aqueous media, the same pore(s) are negatively charged. These findings were also verified by measuring current-voltage curves in a propylene carbonate, $LiClO_4$ concentration gradient. The electroosmotic velocity of the particles also

revealed that the positive zeta potential of the pores in propylene carbonate is significantly higher than the negative zeta potential in water.

Additionally, conically shaped pores, 4-25 nm (tip), 700-1100 nm (base) diameter, KCl and bulky chromium, trivalent (Cr^{3+}) cations, were used to probe the switching of the PET surface potential through *charge inversion*. Briefly, *charge inversion* occurs when a (negatively charged) pore is placed in contact with oppositely (positively) charged multivalent ions at a sufficiently high (≥ 2) Z and bulk electrolyte concentration. At these experimental conditions, the cations attract, over screen and invert the sign of surface potential here, from negative to positive. The origin of *charge inversion* is often described through the concept of a strongly correlated liquid that is formed by the multivalent ions in contact with the charged surface. When the surface potential of the pore is inverted, the observable current-voltage curve changes as well and can be experimentally probed. In this work, it was successfully demonstrated through recorded current-voltage curves and ion current signal measurements in time that when the bulk Cr^{3+} concentration reached 1 mM, the walls of the conically shaped nanopore became positively charged. Also, pores whose tip diameter is less than or equal to 10 nm exhibited ion current fluctuations in time and negative incremental resistance(s). This finding suggests that the pores become partially sterically occluded with the bulky ions which in sub-5 nm pores has major implications on charge inversion and the pore ionic conductance.

Chapter 1.
With Respect to Biology: Pores in Nature

In our (the Siwy) laboratory, we draw a lot of inspiration for our research from nature and the functioning of biological systems. More specifically, ion channel proteins embedded in cellular membranes.

In our bodies, ion channels allow for the highly selective transport of ions (e.g., Na^+, K^+, Ca^{2+} or Cl^-) across cellular membranes in response to stimuli resulting in rapid changes of the osmolar concentration. Some examples of stimuli include the physical deformation of surrounding environments, the binding of ligands or molecules like acetylcholine to ligand-gated channels[1–3], and changes to the membrane potential caused by the opening of voltage-gated ion channels.[4,5] Proper functioning of ion channels helps regulate intrinsic physiological processes[6], serves as the basis of chemical, nerve signaling, and has well-defined implications in several prevalent and fatal neurodegenerative disease states.[7–10]

Ion channels are in their most elegant form, natures *nanopores*. Their responsiveness (to stimuli), sensitivity, and selectivity have motivated researchers to create model, biomimetic porous systems as tools to *replicate* and further *elucidate* the underlying mechanisms that *govern* ionic transport at the nanoscale. *This is the main source of motivation for our lab and this doctoral work.*

Biomimetic, channel-like systems have been constructed in synthetic devices. Some of which include polymeric ethylene terephthalate[11–15], Kapton, polycarbonate[16], silicon nitride[17–20], glass pipettes[21–25], silica planar channels[26,27], and carbon nanotubes[28,29]. These materials which can be etched, lithographed, pulled, synthesized, dielectrically broken down, or drilled using focused ion beam or transmission electron microscopy to create meso- and nano- pores of varying diameters, shapes, and geometries.[30] These pores can be used as templates to mimic the electrochemical operational principles and sensitivity of ion channels.[31–33] Though, to date, ion selectivity, particularly between ions of different sizes has been extremely challenging to achieve.[34]

From a chemical perspective, the small size, high surface area to volume ratio and tunable surface charge of these porous man-made systems gives them unique and

fascinating transport properties that are dominated by controlling the interface characteristics.[35] Nanopores with excess surface charges for example, can induce ionic selectivity such that negatively (positively) charged pores will transport mostly positive (negative) ions.[36] Conversely, mesopores again, with excess surface charges, are responsible for electrokinetic phenomena like electroosmosis.[37,38] Additionally, the presence of surface functionalities, like carboxyl groups, leaves the pores amenable to chemical modification such as the attachment of charges[39–41], specific recognition agents[42,43], charge patterns[44,45] and hydrophobic groups[46,47] which at will, fine tune the surface-interface dominated transport properties.

These transport properties with un/modified pores also make them extremely attractive for a variety of different applications. Some of which include, but are not limited to the creation of ionic circuit elements[33,40,44,48–54], the development of new low detection limit, chemical sensing platforms, including DNA and protein sequencing [22,55,64–73,56–63], separation systems (e.g. desalination)[74,75], and for the purposes of this work, probing the electrochemical properties of solid-liquid interfaces to gain further insight into fundamental ionic transport in aqueous and organic media[25,37,39,41,76,77]. To better investigate the solid-liquid interfaces in aqueous and organic media warrants the development and ratification of techniques capable of making sensitive, selective electrochemical measurements.

The dissertation written herein will discuss some of the tools and techniques that facilitate the systematic studying of solid-liquid interfaces in single polymer porous systems. It is the author's hopeful intention that the topics and ideas introduced here will be used as a paradigm for addressing some of the questions posed as they pertain to ionic transport, and most importantly, the structure of the solid-liquid interface in aqueous and organic media which will hopefully drive analytical, quantitative decision making during the development of dynamic solutions.

Below is a brief description of the information presented in each chapter:

First, Chapter 2 gives details about the track-etched, PET pores used in this project. Chapter 3 & 4 provides background details on the electrical double layer and modes of transport through track-etched pores, respectively. In Chapter 5, conically shaped (nano)pores, bulky chromium, trivalent (Cr^{3+}) cations and sulfate (SO_4^{2-}) anions are used

to probe the switching of the surface potential through *charge inversion*. In Chapter 6, the resistive-pulse technique is used to investigate the electroosmotic transport of unfunctionalized polystyrene particles through the (meso)pores in organic, propylene carbonate solutions of $LiClO_4$. And finally, Chapter 7, summarizes the main points, discusses the results of this doctoral work, and presents planned future work.

Chapter 2.

Pores As Tools to Probe Interfaces: Single Pore Fabrication

For the purposes of this work, 12 μm long poly(ethylene terephthalate) (PET) (Figure 2.1) pores will be the tool of choice for investigating the solid-liquid interfaces.

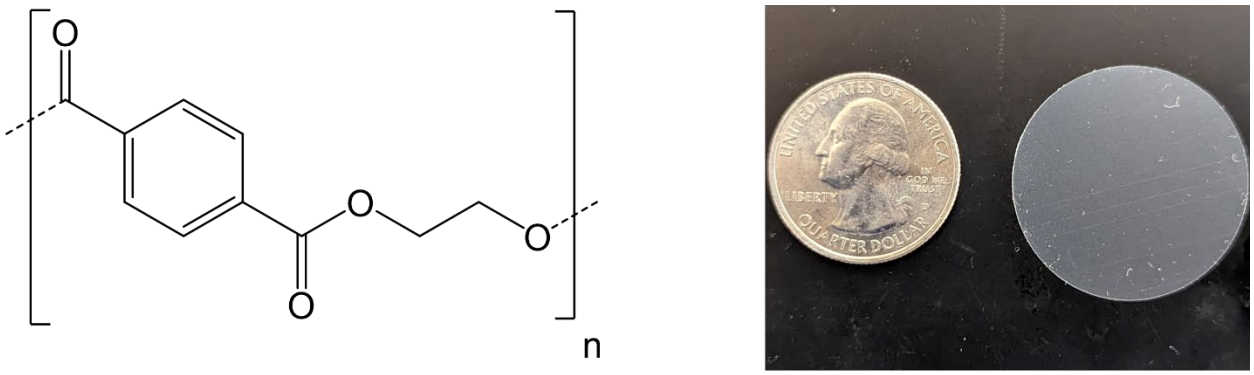

Figure 2.1. Chemical structure and picture of a PET foil irradiated with a single ion track. The foil is 12 μm thick and 3 cm in diameter. The ion track is restricted to a 100 μm diameter region at the center of each foil using a metal aperture mask during the irradiation process.

Commercially available PET films (Hostaphan RN12, Hoechst) are fabricated into pores using the track-etching technique.[41,78–82] The track-etch fabrication technique consists of 3 discrete steps: (1) latent damage track formation, (2) wet chemical etching, and (3) current-voltage characterization (Figure 2.2).

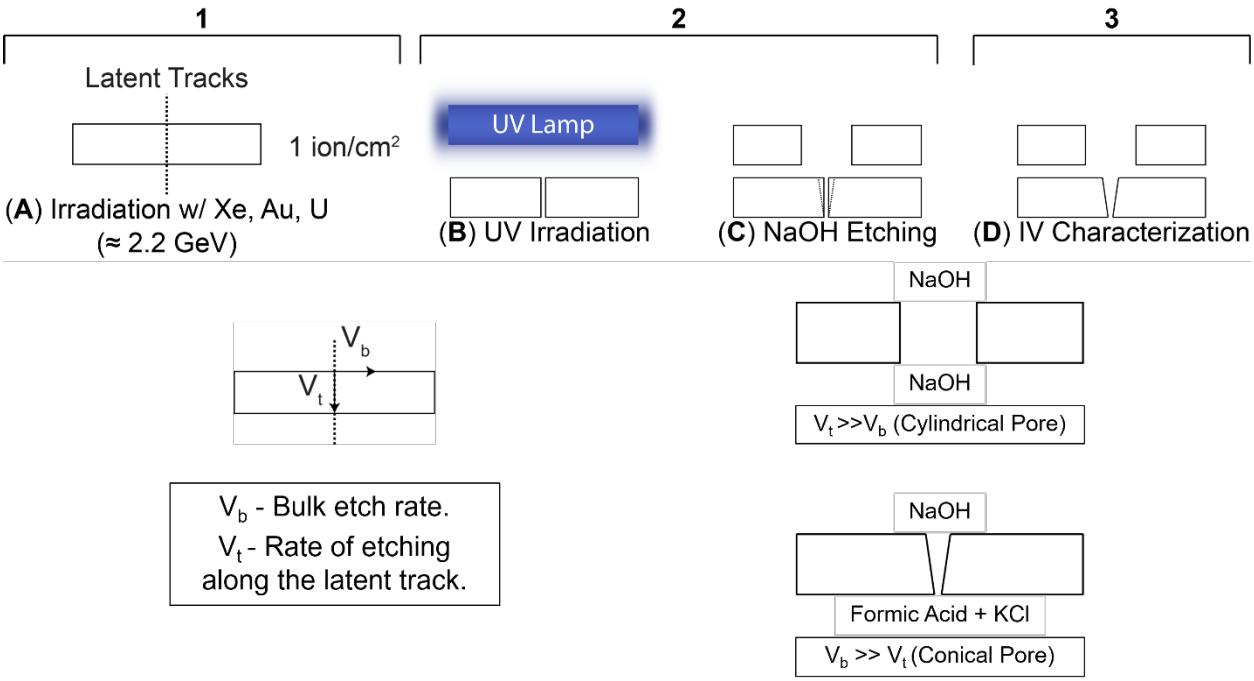

Figure 2.2. Schematic of the cylindrical and conical PET pore fabrication process. (A) Irradiation of PET film with an energetic single, swift, heavy ion, (B) additional long (365 nm) wavelength ultra-violet irradiation, (C) wet chemical etching. By controlling the bulk and latent track etching rates, V_b and V_t respectively, can we allow for different pore geometries to be fabricated, and lastly (D), electrochemical current-voltage characterization using linear sweep voltammetry.

2.1. Latent Damage Track Formation

In track-etch pore fabrication, 3 cm (diameter), stacks of 12 μm thick PET foils are irradiated with swift, heavy, energetic, U^{+35}, Xe^{+18} or Au^{+23} ions with a total kinetic energy of ≅ 2.2 GeV at the GSI Helmholtzzentrum für Schwerionenforschung (GSI Helmholtz Centre for Heavy Ion Research) in Darmstadt, Germany (www.gsi.de). The Institute for Heavy Ions Research has unique instruments, more specifically, a UNILAC: Universal Linear Accelerator, capable of irradiating films with a known number of ions. Depending on the fluence of the ion beam created at the UNILAC, each PET foil can be irradiated with 1 - 10^{10} ions/cm^2. The number of ions that penetrate the films during this irradiation process determines the number of pores created during the chemical etching process. Therefore, irradiation with one heavy ion will lead to the preparation of a single-porous membrane system. Single, heavy ion irradiation is also achieved by placing a metal, 100

μm aperture mask in front of the stacked foils. Additionally, the linear particle accelerator at UNILAC is magnetically defocused to decrease the flux of ions so that on average, only one heavy ion per second passes through the films and mask aperture. Once the heavy ion is detected on the opposite side of the stacked foils, the particle accelerator is shut down. This irradiation process creates the formation of a single, localized, thin (< 20 nm diameter)[83], cylindrical latent damage tracks through each 6-film stack of 12 μm thick PET foils. Once irradiated, each individual PET foil is (wet) etched chemically at UCI where the desired shape and geometry of each pore is controlled with nanometer precision.

2.2. Chemical Etching

Prior to chemical etching, each individual PET film is subjected to additional irradiation. This time, from a compact UV lamp. Every PET foil is irradiated with long (365 nm) wavelength ultra-violet light for one hour on each side of the film. The mechanism of this ultra-violet light irradiation process is not well understood. Though, it has been found that the reproducibility and successfulness of fabricating pores is increased when this step has been performed.[84,85]

2.2.1 *Cylindrical PET Pores*

The conditions of the chemical etching process determine the shape and size of the pores. Symmetric etching of the 12 μm thick PET foils along the latent damage track (V_t) in 2 M NaOH solution heated to a temperature of 60 °C creates pores that are known to have a nearly ideal cylindrical geometry. The average pore diameter increases linearly with etching time. The laminar, semi-crystalline structure of PET leads to inhomogeneities of the local pore diameter with an amplitude up to ~20% of the pore diameter.[78,79] These inhomogeneities (undulations) result in the formation of a nonuniform electric field inside the pore when voltage is applied across the membrane. These undulations make the pore sensitive to the shape of passing objects when used in pore analytics.[79,80]

2.2.2 *Conical PET Pores*

Conversely, asymmetric etching of the irradiated PET film along the radial axis of the latent damage track (V_b) leads to the formation of a well-approximated tapered-cone (conically) shaped pore whose small tip diameter can be as small as a few nanometers, and large base diameter (on the other side), is on the micrometer scale.[49] One side of the

pore is placed in contact with 9 M NaOH, and the other side, with a 1 M Formic Acid, KCl (STOP) solution. Bare platinum electrodes were placed in opposing chambers of a custom-built, polychlorotrifluoroethelyne (Kel-F), conductivity cell with an irradiated, single 12 μm thick foil mounted between the chambers. The (working) platinum electrode was placed into the chamber of the conductivity cell containing the 9 M NaOH. This side would eventually become the large base opening of the pore and the (ground) platinum electrode, which was placed into the chamber containing the STOP solution, the small tip opening of the pore. This placement of the working and reference electrodes were kept the same for all the electrochemical measurements performed hereafter. Measurable breakthrough of the faradaic, transmembrane current (~ 300 pA) when 1 V was applied across the film indicated etching success. Once etched, the pores, cylindrical or conical, were left overnight in MilliQ water before being sized.

2.3 Pore Sizing

Prior to experimentation, the opening diameter(s) of each PET pore was measured using a well-established, non-destructive technique based on electrochemical characterization. Current-voltage (i-V) measurements in unbuffered 1 M KCl were used to measure the pore conductance and subsequently, calculate the pore diameter (Figure 2.3). The voltage was changed from -1 V to +1 V with 100 mV steps for cylindrical pores and from -0.1 to +0.1 V with 10 mV steps for conical pores using Ag/AgCl electrodes (in-house chlorinated Ag wire). These electrodes were placed in opposing chambers of the conductivity cell with the etched (cylindrical or conical) PET pore membrane mounted between the chambers. The potential window for conical pores was chosen to ensure that a linear conductance was obtained for quantification of the pore conductance (G). Once the experimental set-up was complete, a linear potential sweep was applied to the working electrode for 1 (forward) cycle. The current generated from the forward (oxidation) scan was constructed into an i-V curve, and the slope, provided the conductance of the electrolyte-filled pore. Electrochemical sizing measurements were performed in high electrolyte concentrations where the length of the electrical double-layer is thin (~ 0.3 nm for 1 M KCl). At high electrolyte concentrations, we assume that the conductivity of the electrolyte solution inside the pore is comparable to that of the bulk solution.

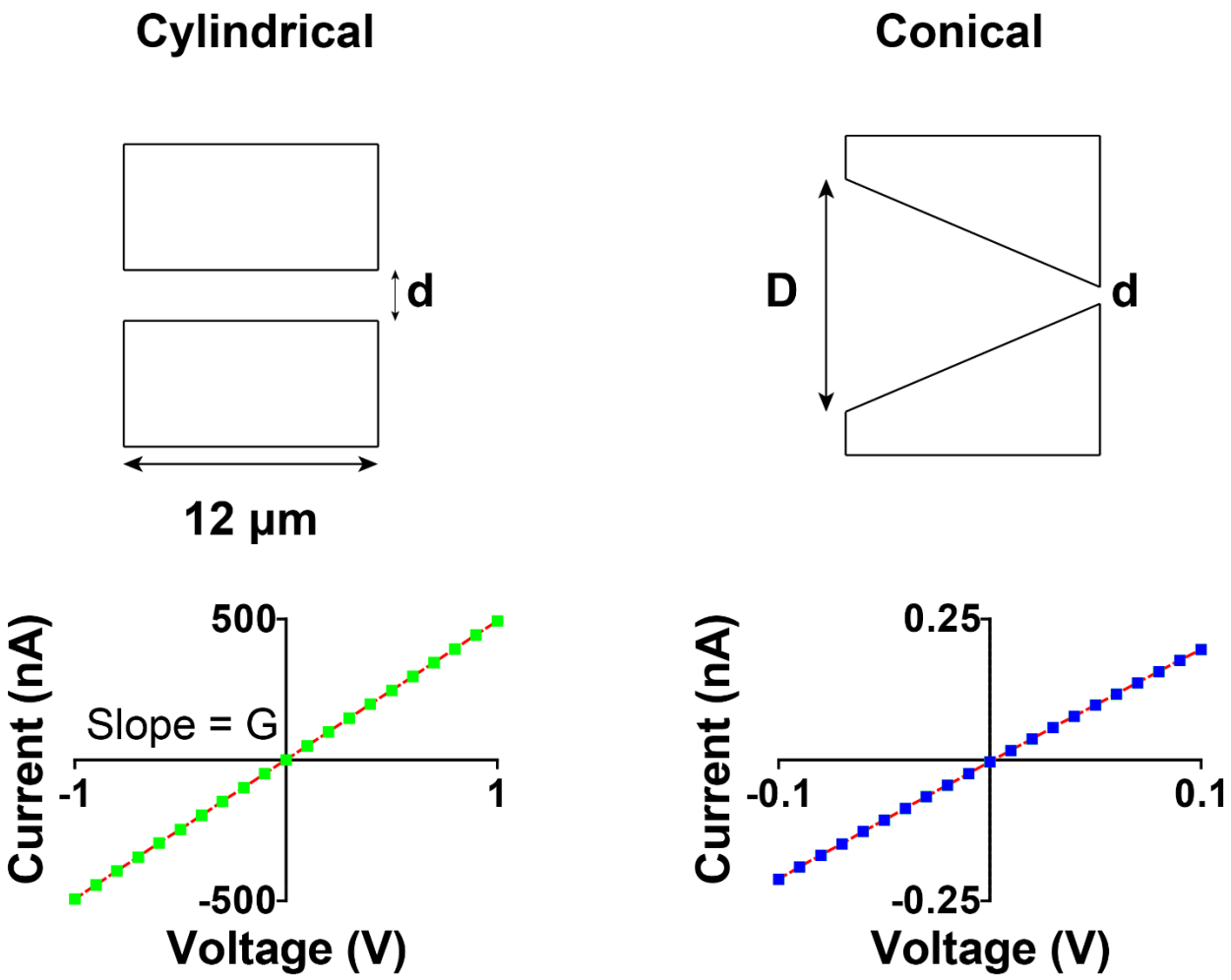

Figure 2.3. Current-voltage curves of the linear dielectric approximation for the conductance of a single cylindrical (left) and conical (right) pore in 1 M KCl. From the measured conductance the opening and small tip diameters of each pore can be calculated. Here, the cylindrical pore has an opening diameter of 820 nm and the conical pore, a small tip opening of 4 nm. For conical pores, D, here 720 nm, is determined by the elapsed etching time and bulk etch rate: 2.13 nm/min at 20 °C in 9 M NaOH.[49]

2.3.1 *Cylindrical PET Pores*

For cylindrical pore geometries, it is possible to simply model the pore as a linear dielectric material i.e., a cylindrical resistor and solve for the pore diameter using the equation[86]:

$$G = \frac{\kappa A}{l} \qquad \text{eq. (2.1)}$$

where: κ is the solution conductivity (10 Siemens/m for bulk 1 M KCl), A, the cross-sectional area, and l, the pore length. Substituting for the cross-sectional area of a cylinder and solving for d, the pore radius, we now obtain the equation:

$$d = \sqrt{\frac{4lG}{\kappa\pi}} \qquad \text{eq. (2.2)}$$

For the electrochemical sizing of cylindrical PET pores.

2.3.2 *Conical PET Pores*

For conical pores however, the approximation that is used instead is that of a resistor formed by the intersection of a cone with a spherical shell.[87] This approximation is more accurate for small angles of the cone opening. G is related to the small tip radius (d) of the pore from the equation:

$$d = \frac{4lG}{\kappa\pi D} \qquad \text{eq. (2.3)}$$

The large base opening diameter, D, is calculated from the bulk-etch rate of PET: 2.13 nm/min at 20 °C in 9 M NaOH.[49] D is determined using the equation:

$$D = 2 * 2.13 * t \qquad \text{eq. (2.4)}$$

Where t is the total etching time (minutes).[49] The bulk-etch rate was verified using imaging, more specifically, scanning electron microscopy (SEM).[88] However, due to the large surface area of the PET films and the presence of only one pore, sizing of the pores using SEM would be extremely difficult to measure and determine experimentally.

2.4 Chemical Modifications

Track-etched PET pores are amenable to chemical modification[15,40,44,89–91] due to the presence of a highly dense surface carboxyl group network on the pore walls at a density of ~1 carboxyl group per nm^2.[92] The carboxyl groups form because of alkaline hydrolysis induced during the wet chemical etching step[93] (Figure 2.4). The pKa of the surface carboxyl groups of PET is ~3.5.[92] In solutions at pH's > 4, the pore walls are negatively charged. Thus, a variety of chemical modifications can be performed to give the pore(s) special and unique transport properties.[47,56,94] One that was used extensively throughout this work, includes the use of a positive polyelectrolyte: poly(allylamine hydrochloride)

(PAH) which electrostatically adsorbs itself to the negatively charged carboxyl groups and renders the PET pore with a positive surface potential. The amine-terminated functionalities of PAH have a pKa of 9.5.[40] Therefore, in solutions at pH's > 4, we expect a pore that has been modified with PAH, to have a positive surface charge. This PAH modification was extremely useful in being used as a guideline that aided and facilitated the interpretation of each experimental result where the chemical properties of the pore walls were tuned using aqueous, multivalent, and organic media.

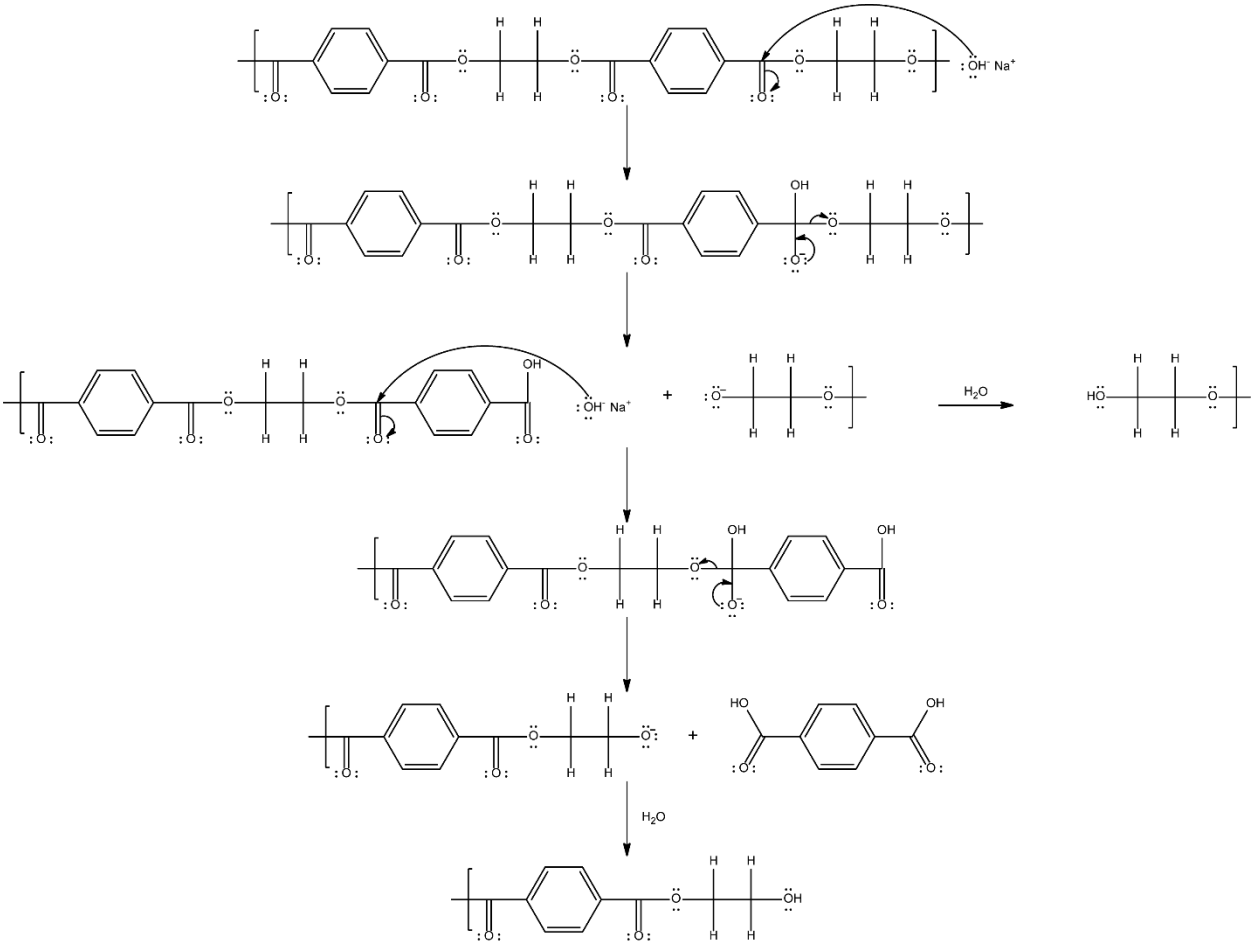

Figure 2.4. Depolymerization of PET by alkaline hydrolysis. Sodium hydroxide (NaOH) attacks the ester bonds of the polymeric chain and sequentially removes the constituent pieces of the PET monomer ethylene glycol and terephthalic acid.[95,96]

Chapter 3.
The Electrical Double Layer

3.1. The Classical Depiction of the Electrical Double Layer

Pore walls of track-etched PET pores with negative, surface carboxyl groups (as prepared) can often be modeled by a charging parallel plate capacitor.[37] When exposed to an electrolyte solution at equilibrium, i.e., in the absence of external forces influencing transport, an array of countercharged species (cations) accumulates at the area closest to the pore-solution (solid-liquid) interface surface to electrostatically offset the charged surface potential and as a result, the electrical double layer is formed.

The solution side of the electrical double layer is made up of several “layers” (Figure 3.1). The first, closest to the pore walls, are the immobile, specifically adsorbed counterions of the Stern layer.[97] Next, a diffuse layer of nonspecifically adsorbed ions extends from the Stern layer into the bulk solution. The diffuse layer encompasses the Debye length (λ_D) and the shear plane.

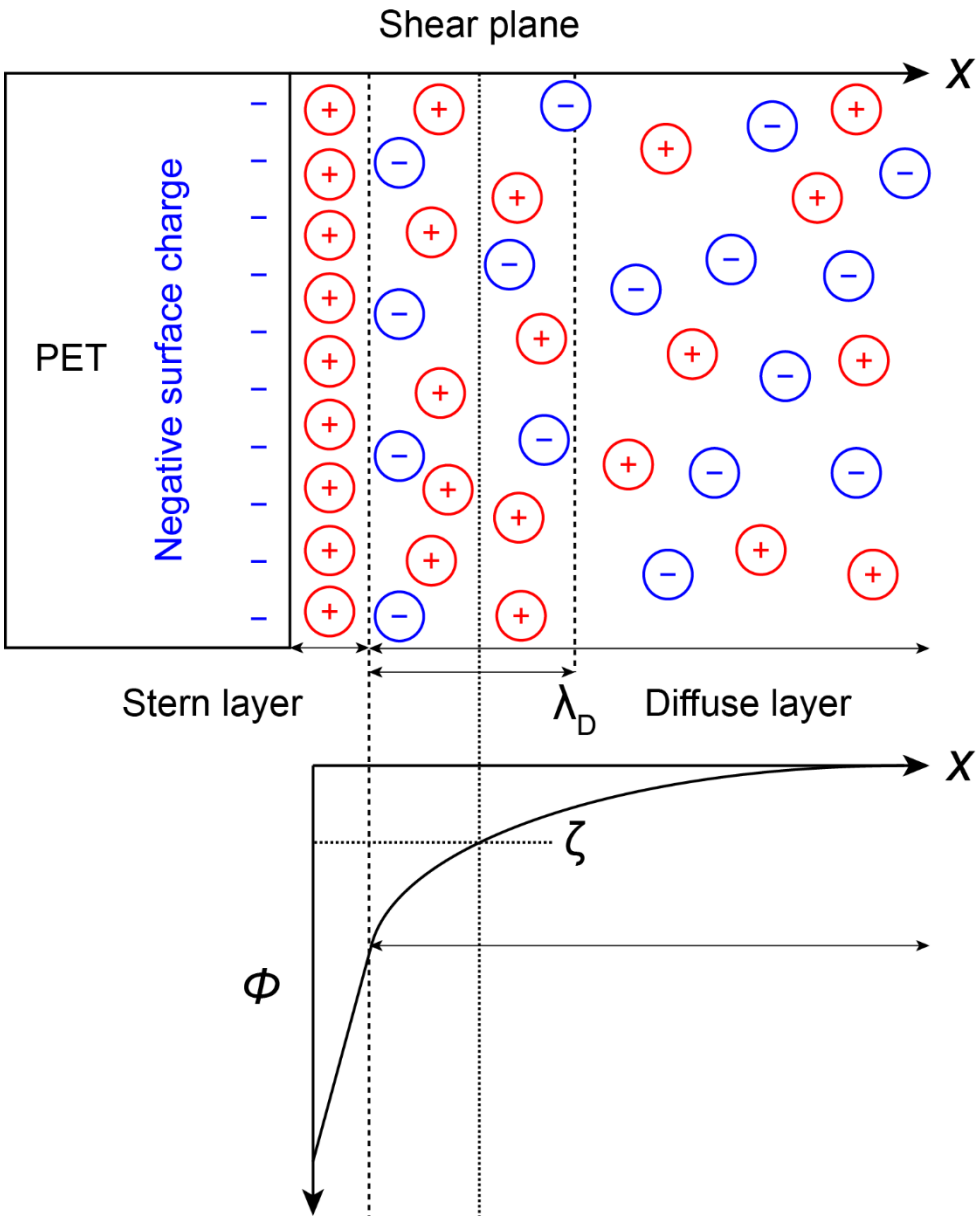

Figure 3.1. The classical, Gouy-Chapman-Stern depiction of the electrical double layer which encompasses the Stern layer, Debye length and Shear plane. The electrostatic potential (φ) which describes the ion distribution along a (negatively charged) pore wall is plotted along the x-axis and is mathematically illustrated by the Poisson-Boltzmann equation.

The Debye length is a concentration dependent property of the bulk electrolyte solution and provides the characteristic length scale at which electrostatic interactions are

screened, and the potential of the pore wall decays 1/e times. The Debye length is given by the equation:[37]

$$\lambda_D = \sqrt{\frac{\varepsilon_0 \varepsilon_r k_B T}{\sum_j (z_j e)^2 c_j}} \qquad \text{eq. (3.1)}$$

where: ε_0 is the permittivity of free space, ε_r, the dielectric constant, k_B, the Boltzmann constant, T, temperature, z_j is the ion valency, e, the elementary charge of an electron, and c_j, the molar concentration of ion j. For a dilute aqueous (ε_r = 78.49), 1:1 electrolyte solution at 25 °C, this equation can be simplified to:

$$\lambda_D = \frac{0.3\ nm}{\sqrt{c_j}} \qquad \text{eq. (3.2)}$$

$[c_j]$ is in moles/liter (M). As an added example, λ_D in 100 mM KCl is ~ 1 nm.

The shear plane, conversely, is the point at which the fluid of the electrical double layer becomes "mobile" and shows elastic behavior relative to the stationary pore wall. The value of the electrical potential at the shear plane is the zeta (ζ) potential. The ζ is an extremely very convenient way to characterize and measure the surface charge density of the pore walls.

Figure 3.1 shows the electrical double layer which includes the Stern layer, shear plane, Debye length, and diffuse layer. In this the traditional Gouy-Chapman-Stern model of the electrical double layer, the distribution of local electric potential, charge distribution and ionic concentrations next to a charged surface is often described by the solution to the combination of the Poisson:

$$\nabla^2 \varphi = \frac{-\rho_{charge}}{\varepsilon_r \varepsilon_0} \qquad \text{eq. (3.3)}$$

And Boltzmann (distribution):

$$c_j = c_{0(j)}\, \mathrm{e}^{\frac{z_j e\varphi}{k_B T}} \qquad \text{eq. (3.4)}$$

equations resulting in:

$$\varphi(x) = \varphi_0 e^{-\frac{x}{\lambda_D}} \qquad \text{eq. (3.5)}$$

where: ρ_{charge}, is the net charge density in the system, and $c_{0(j)}$, the bulk concentration of ion j. Mind, the relation in eq. (3.5) is only a good approximation at low potentials, i.e., when $\varphi_0 \leq 50/z$ mV at 25 °C.[86] It's from this framework that we begin to ask questions about the structure of the electrical double layer when PET pores are exposed to aqueous solutions containing multivalent ions and organic solvents. When exposed to these solution matrices, the structure of the electrical double layer changes to great effect and forms the basis of this doctoral work. We will discuss the implications of introducing each to our system beginning with multivalent ions:

3.2. Non-Classical Electrical Double Layers

3.2.1 *Multivalent Ions*

The Poisson-Boltzmann equation is a simple classical mean field theory that often ignores the correlation amongst ions and charged surfaces.[9812,99] When a charged surface comes in contact with a critical concentration of multivalent counterions that over screen and invert the native charge, a phenomena known as charge inversion occurs. As an example, a surface with carboxyl or silanol groups become effectively positively charged when in contact with calcium (II) or cobalt (III) ions.[12,100] In nanopores, charge inversion induces a switch between cation selectivity in negatively charged nanopores with monovalent salts such as NaCl or KCl, to anion selectivity using multivalent cations.[101] Ubiquitous in nature, charge inversion is important in processes such as DNA condensation, viral packing, and colloidal coagulation. [99,100,102–107]

The accumulation of counterions on the surface is possible through the spatial correlation of counterions that lowers the system's potential energy and overcomes electrostatic repulsion.[99] The adsorbed counterions have been postulated to form a strongly correlated liquid, like the structure of a Wigner crystal.[99,108] This spatial organization of multivalent counterions has been directly observed under electron microscopy.[109] Thus far, the research on charge inversion has been focused primarily on finding the experimental conditions where overcharging occurs in nanopores and nanofluidic channels. Measurements of electrokinetic phenomena such as streaming current[100], open circuit potential[101] and current-voltage (i-V) curves[12,106,110], have identified the critical concentration needed to switch the sign of the effective surface charge. However, very little is known about how the onset of charge inversion influences ionic transport. Especially in nanopores whose opening diameter is comparable to the size of the multivalent ions (Figure 3.2).

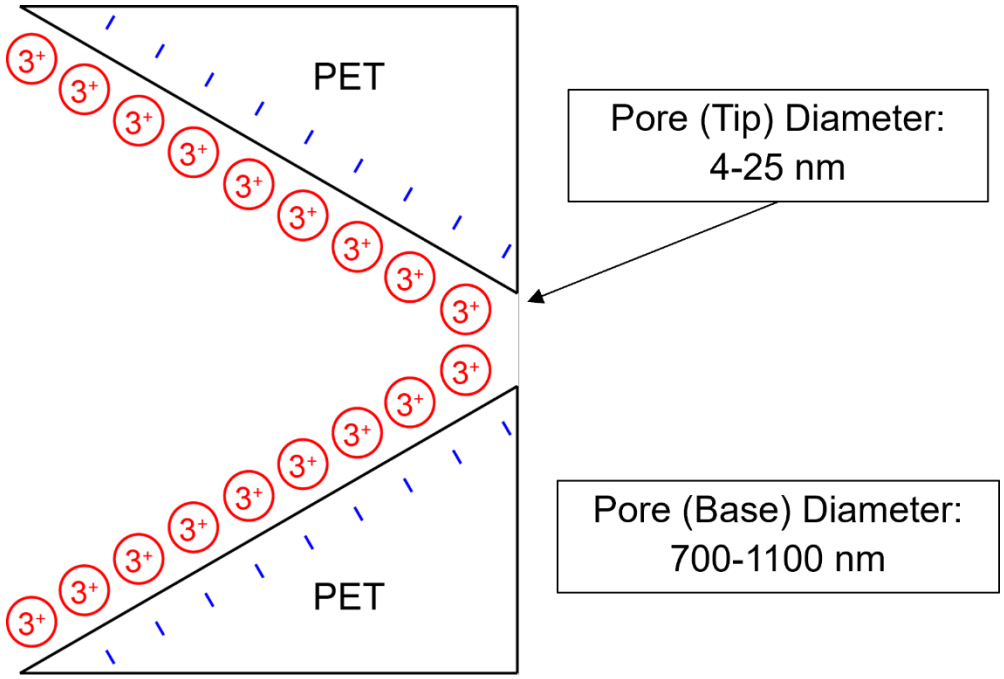

Figure 3.2. The structure of the electrical double layer when oppositely charged multivalent (here, trivalent) ions are exposed to the (negatively charged) PET surface. The multivalent ions form a strongly correlated liquid of the trivalent ions which depending on the bulk electrolyte concentration will over screen and invert the sign of the pore surface potential from negative to positive.

3.2.2 *Organic Solvents*

Additionally, it has been shown that organic solvents such as acetone, acetonitrile, and propylene carbonate, independent of the material used during experimentation, can render a material positively charged even though in water, the material is negatively charged.[39,41,76] All these organic solvents are polar and aprotic. Therefore, they are not expected to participate in any Brønsted-Lowry acid-base reactions with the surface carboxyl groups of an as prepared PET pore (as an example), to change its surface charge. It has been postulated that the positive surface charge in these organic solvents originate from the reorganization of the solvent molecules at the solid-liquid interface.[25,111] These ordered solvent molecules form a “bilayer” along the solid interface and specifically adsorb cations (e.g., Li^+) from the electrolyte solution (Figure 3.3). Since the location and density of the adsorbed cations are not limited by the specific chemical, e.g. carboxyl groups on the pore walls, it is possible that the surface (negative) charge is screened differently from the adsorbed cations than what was previously predicted by the Poisson–Boltzmann equation.[39]

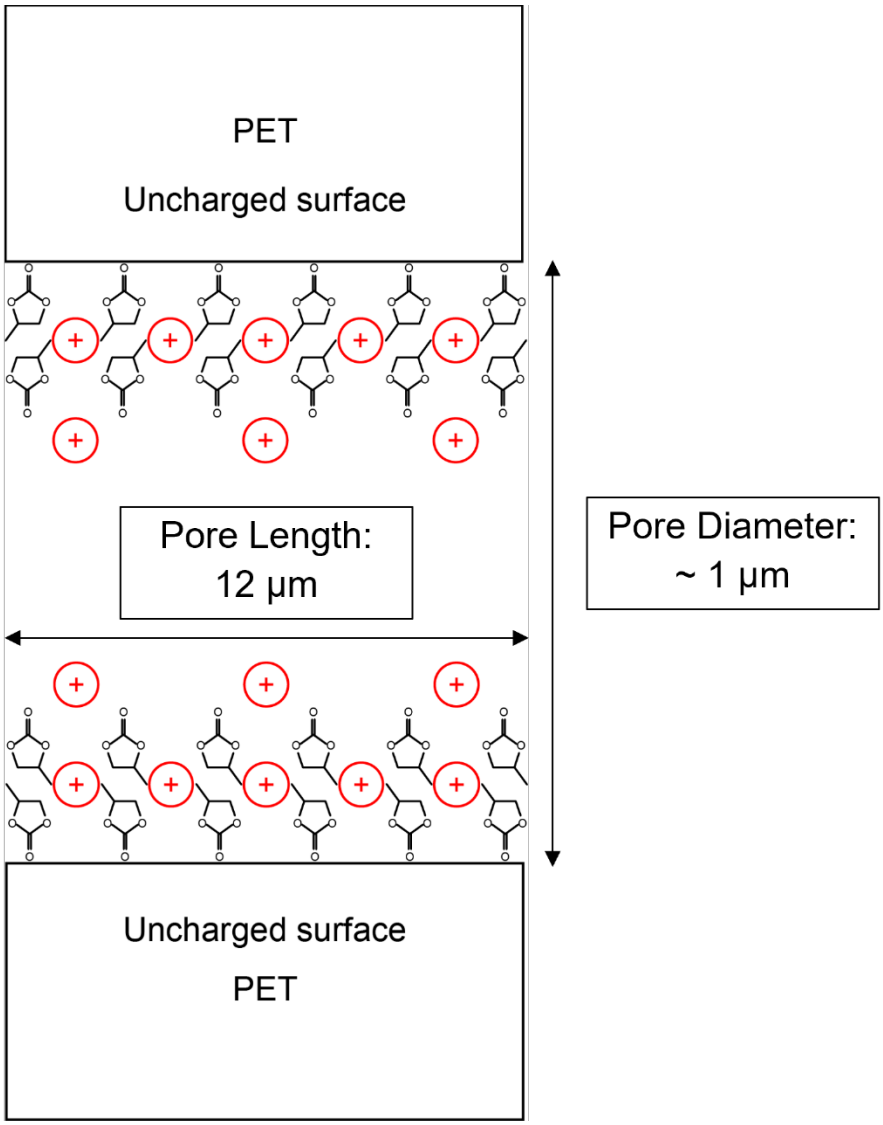

Figure 3.3. The structure of the electrical double layer when organic solvents (here, propylene carbonate) are exposed to an assumed uncharged PET surface. The propylene carbonate solvent molecules form an ordered “bilayer” along the pore wall and specifically adsorb cations from the electrolyte solution to invert the sign of the pore surface potential from negative in aqueous solvents to positive in propylene carbonate and other organic solvents.

Chapter 4.
Modes of Transport Through Pores

4.1. The Nernst-Planck-Stokes Equation

To understand how ions are transported through pores, we first must consider mass transport. The Nernst-Planck-Stokes equation describes the movement and rate of species through the pore in response to a chemical, electric, or hydrodynamic gradient.

Since the measured resistance of a single PET pore is typically in the M Ω regime (measured from an i-V curve of a ~800 nm diameter pore), its resistance dominates over those in the electrochemical system (conductivity cell bath, Ag/AgCl electrodes). Additionally, because of the pores' high aspect ratio (pore: length/diameter), the access resistance of a single pore accounts for < 1% of the total resistance in accordance with the equation:[112,113]

$$\frac{1}{4d\kappa} \qquad \text{eq. (4.1)}$$

where κ is the solution conductivity and d, the pore radius. Therefore, in our equivalent circuit model of the electrochemical conductivity cell, we only consider the ion current passing through the volume of the pore. The experimentally measured ion current is directly proportional to the number of charge carriers in the pore[86] and the flux density given by the Nernst-Planck-Stokes equation:

$$\boldsymbol{J}_{j,Total} = -D_j \boldsymbol{\nabla} C_j - \frac{z_j F}{RT} D_j C_j \boldsymbol{\nabla} \varphi + C_j \boldsymbol{v} \qquad \text{eq. (4.2)}$$

for the generalized form of the equation.[37,86,114–116] $\mathbf{J}_{j,Total}$, the flux density, is the number of moles of species j being transported through the pore per unit area in a three-dimensional Cartesian space:

$$\boldsymbol{\nabla} = \boldsymbol{i}\frac{\delta}{\delta x} + \boldsymbol{j}\frac{\delta}{\delta y} + \boldsymbol{k}\frac{\delta}{\delta z} \qquad \text{eq. (4.3)}$$

for linear (one-dimensional) mass transfer, $\boldsymbol{\nabla}$ = $\mathbf{i}(\delta/\delta x)$, $\mathbf{j}(\delta/\delta y)$, or $\mathbf{k}(\delta/\delta z)$ where i, j, or k are the unit vectors along their respective axes and x, y, and z are their distances. C_j is the concentration of species j within the pore.

Treating each term independently, the modes of mass transport are: (1) diffusion, the movement of a species under the influence of concentration gradient. Derived from Fick's first law, diffusion states that at equilibrium, the diffusive flux density of species j is proportional to the concentration gradient ∇C_j and D_j, the diffusion coefficient of species j. (2) Migration, the movement of a charged species under the influence of an electric potential gradient ($\nabla\varphi$). Z_j, is the charge of species j. R is the molar gas constant, F, Faraday's constant, and T, the temperature. The migration rate (v_{ep}) of an ion in an electric field is equal to the product of the field strength (E) and the electrophoretic mobility (μ_j^{ep}):[117]

$$v_{ep} = \mu_j^{ep} E \qquad \text{eq. (4.4)}$$

where μ_j^{ep} is equal to:

$$\frac{q_j}{f} \qquad \text{eq. (4.5)}$$

where q_j is the ionic charge of species j. μ_j^{ep} is proportional to q_j and inversely proportional to the frictional retarding forces (f). The governing frictional forces in liquids is expressed by the Stokes equation (f) where r_j is the ionic radius of species j and η, the solution viscosity:[117]

$$f = 6\pi\eta r_j \qquad \text{eq. (4.6)}$$

(3) Convection, the movement of a species under hydrodynamic transport. **v** is the convective velocity field with which a volume element in solution moves. Hydrodynamic transport (convection) can be characterized as either natural (density gradient) convection, forced (pressure gradient) convection, or in pores, electroosmotic transport due to an applied electric field.[37]

The full set of Poisson-Nernst–Stokes are extremely difficult to solve analytically. Numerical solutions are often provided; however, electrochemical systems are designed so that one or more of the contributions to mass transfer are negligible. For the purposes of this work, we typically negate diffusion and mostly consider the migration and electroosmotic convection components.

4.2. Electroosmosis

In the presence of an electric field, without a concentration gradient (diffusion), solvated counterions within the diffuse layer: cations (negatively charged pore walls) or anions (positively charged pore walls) are attracted to the negatively or positively biased working electrode and subsequently, drag the bulk electrolyte fluid and any analytes within, from one side of the membrane across the volume of the pore. Because of viscous coupling, the bulk electrolyte liquid is pumped through the pore and creates an electroosmotic (EOF) uniform flat “plug like” flow profile of the solution migrating towards the biased working electrode (Figure 4.1).

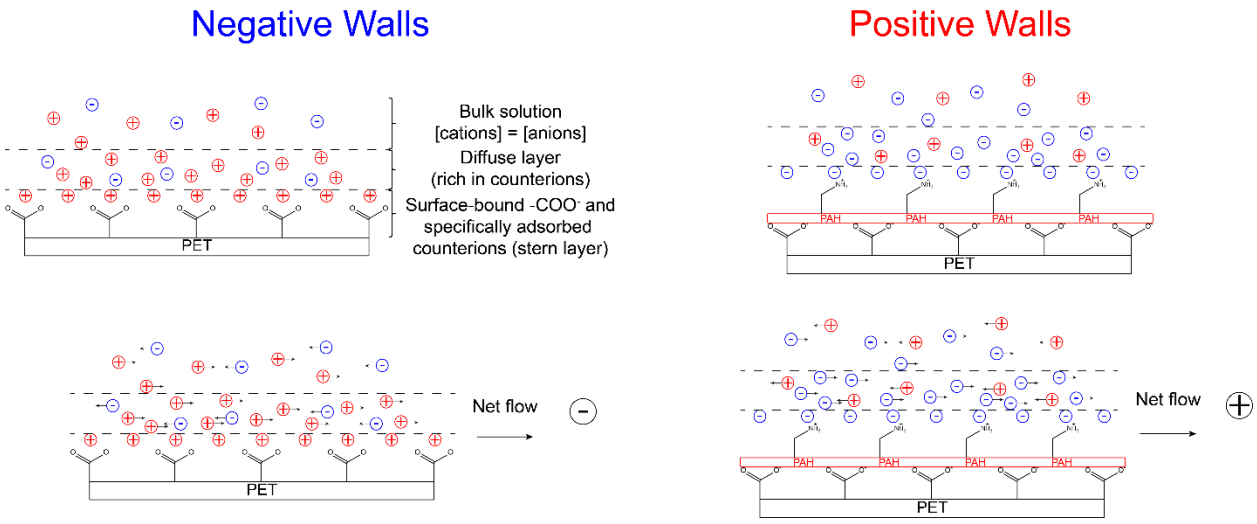

Figure 4.1. The electrical double layer created by a negatively charged, as prepared (left), and a positively charged, PAH modified (right) PET pore with nearby cations (as prepared) and anions (modified). The predominance of cations (anions) in the diffuse layer produces a net electroosmotic flow towards the negatively (positively) biased working electrode when an external (electric) field is applied.

Equation (4.7) describes the electroosmotic radial velocity flow profile in pores with thin electrical double layers.[36,118,119]

$$u(x) = \frac{\varepsilon_0 \varepsilon_r E}{\eta}(\varphi(x) - \zeta) \qquad \text{eq. (4.7)}$$

where: u is the streamwise velocity, E, the electric field strength (V/L)[39,117], ε_0 is the permittivity of free space, ε_r, the dielectric constant, φ is the electrical potential (at distance

x from the charged pore walls), and ζ, the zeta potential. Equation 4.7 suggests that the electroosmotic velocity flow profile is constant (flat) in large pores since the interior has zero electric potential.

4.3. Approaches to Answering Questions Regarding Transport

In our discussion thus far, we have introduced cylindrical and conically shaped PET pores, our model systems to probe solid-liquid interfaces, and several important concepts in the fields of biophysics and electrostatics. Although there are a variety of electrochemical measurement techniques researchers have employed to probe and study changes in the structure of the solid-liquid interface, like current-voltage curves and resistive-pulse sensing[25,37,39,41,76,77], there is always a need to continuously advance our analytical and technological toolkit, especially when the solid-liquid interface is studied under nanoconfinement. By doing so, researchers can continue to ask and answer questions about what the structure of the solid-liquid interface is in aqueous (multivalent ion) and organic media and the consequences they have on transport. Each of the presented approaches here forth are necessary to dealing with and addressing this complex problem beginning in aqueous media with multivalent ions:

Chapter 5.

Solid-Liquid Interfaces in Aqueous Media with Multivalent Ions: Gating of Ion Current with Charge Inversion

5.1. Current-voltage curves of single conical nanopores in monovalent KCl electrolyte solutions

We chose conically shaped PET nanopores[32,33,49,120] with voltage-dependent ionic concentrations as the model system to understand the role of charge inversion in tuning ionic transport under nanoconfinement. A conical nanopore with excess surface charges rectifies ion current such that currents for one voltage polarity are higher than currents for the opposite polarity. In our experimental set-up, the pores were placed between two chambers of a custom-built conductivity cell with symmetric electrolyte concentrations. The working electrode was placed at the large base opening, and the ground electrode, at the small tip opening. An as prepared conically shaped pore with negative surface charges will rectify the ion current and exhibit larger current magnitudes for negative voltages that source cations from the small tip opening of the pore compared to currents of the opposite voltage polarity (Figure 5.1).[32,33,49,54,121] A pore with positive surface charges conversely, will exhibit a current-voltage (i-V) curve that is inverted with respect to the origin point (0, 0) compared to an as prepared pore with negative surface charges. The positive currents will be larger in magnitude than negative currents.

The reason why conically shaped pores rectify ion current is because of the pore shape in combination with the surface charges induce a voltage dependence on the concentration of ions in the volume of the pore.[11,44,54,115] As shown in previous studies[122], the steep increase of the ion current in a negatively (positively) charged pore at negative (positive) voltages originates from the enhanced concentration of cations and anions in the region closest to the small tip opening. However, for positive (negative) voltages, there is a depletion zone of the ions inside the volume of the pore which ultimately limits the cationic (anionic) current flowing through the pore small tip opening. The experimentally obtained i-V curves from the conically shaped pores and the way they rectify are sensitive to changes in the magnitude, and polarity of the surface charge density, pore opening

diameter, and salt concentration which subsequently induces voltage dependent ion selectivity.[21,54,89,123–127] These unique characteristics make conically shaped pores an ideal sensing platform for probing charge inversion and subsequently, the properties of solid-liquid interfaces.

To further exemplify how the surface charge density of a conically shaped pore can be inferred from the direction of rectification, control experiments were performed where the pore was as prepared and modified using a positively charged polyelectrolyte PAH. The sign of the surface charge can be switched by electrostatically adsorbing PAH to the negatively charged pore walls. Attachment of the highly charged molecules led to the inversion of the current-voltage curve that provided evidence of the successful switch of the effective surface charge from negative to positive.[21,44] Figure 5.1 shows the transport properties of a single conically shaped pore before and after the attachment of PAH. i-V curves of a conically shaped pore as prepared (blue trace) and modified with PAH (red trace) were recorded in symmetric electrolyte concentrations of KCl. These recordings in aqueous KCl were used as a guideline that afforded information about the sign of the surface charge density of the pore walls throughout this study with conically shaped pores.

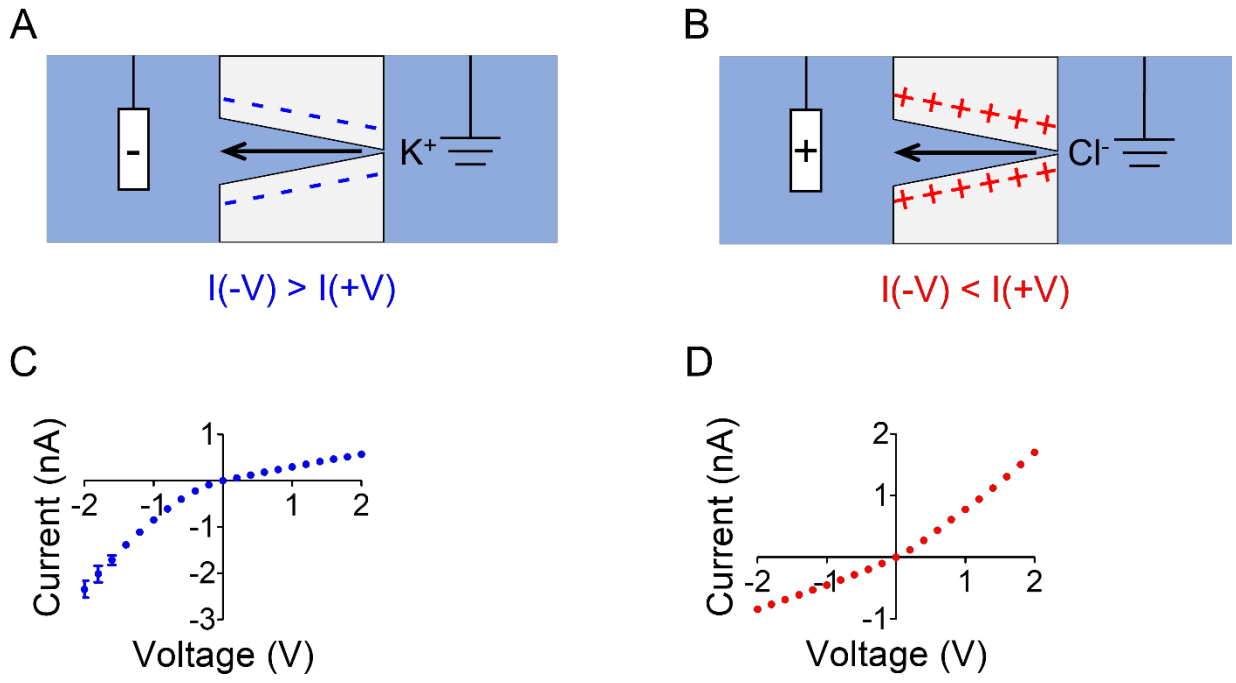

Figure 5.1. Probing surface charges in a single conically shaped pore by measuring current-voltage curves in KCl salt solutions. A pore is placed in a conductivity cell whose chambers (~ 1.5 mL) are filled with 100 mM solutions of KCl. (A, B) Schemes showing ion transport in the pore as a function of polarity, applied voltage and the surface charge. The arrows indicate the direction of cation (A) and anion (B) electrophoretic flow for the voltage polarity that produces higher currents. (A) If a pore carries negative surface charges due to the surface carboxyl groups (blue negative sign), the direction of electrophoresis is determined by the direction of cation migration. At negative voltages, cations move from the chamber containing the ground electrode and electrophoretically fill the volume of the pore. Conversely, at positive voltages, there is a depletion of cations inside the volume. This pore will rectify the current such that negative currents are larger in magnitude than positive currents. (B) A pore with positive surface charges due to amines on the pore walls (red positive sign) will be filled and depleted with anions at positive and negative voltages, respectively. This pore will exhibit higher currents at positive voltages than at negative voltages. The direction of electrophoretic flow in this pore is determined by the migration of anions. (C) Recordings for a 4 nm tip opening and a 720 nm base opening in diameter conically shaped PET pore placed in 100 mM KCl. The blue curve was obtained for the pore as prepared. (D) Recordings for the same 4 nm (tip opening) and 720 nm (base opening) pore after it had been modified with PAH which rendered the pores surface charge positive. All current-voltage curves are averages of three forward and reverse scans. The insets show electrode arrangements that correspond to negative and positive applied voltages, respectively.

Additionally, the ion current characteristics of conically shaped pores are dependent on the salt electrolyte concentration and the small tip opening diameter. Figure 5.2 shows i-V curves for a conically shaped pore with a 14 nm diameter small tip opening in four different concentrations of KCl. In 0.1 mM and 1 mM KCl, the pore rectifies weakly and only in the two highest concentrations (10 and 100 mM), does the pore rectify such that the negative currents are ~ 3 times larger in the magnitude than the positive currents. This non-intuitive dependence of the current rectification on ion concentration was reported before and explained by the inability of the depletion zone to be formed when the electrical double-layer spans over a large portion of the pore cross-sectional area at

the tip region. When the KCl concentration increases from 1 mM to 10 mM, the current at - 2 V increases ~ 5 times while at + 2 V, the positive current only increases ~ 2 times. As the concentration of KCl increases to 100 mM, the currents at both voltage polarities increase by a factor of 2. It is noted that in all cases, the ion current is significantly greater than the calculated value when the pore volume is filled with the bulk solution which in addition to the dependence of the ion current rectification on the bulk electrolyte concentration agrees with previous reports.[123] These findings suggest that the local surface charges at the small tip opening of the pore walls dominate pore transport properties and the extent at which the ion current rectifies.

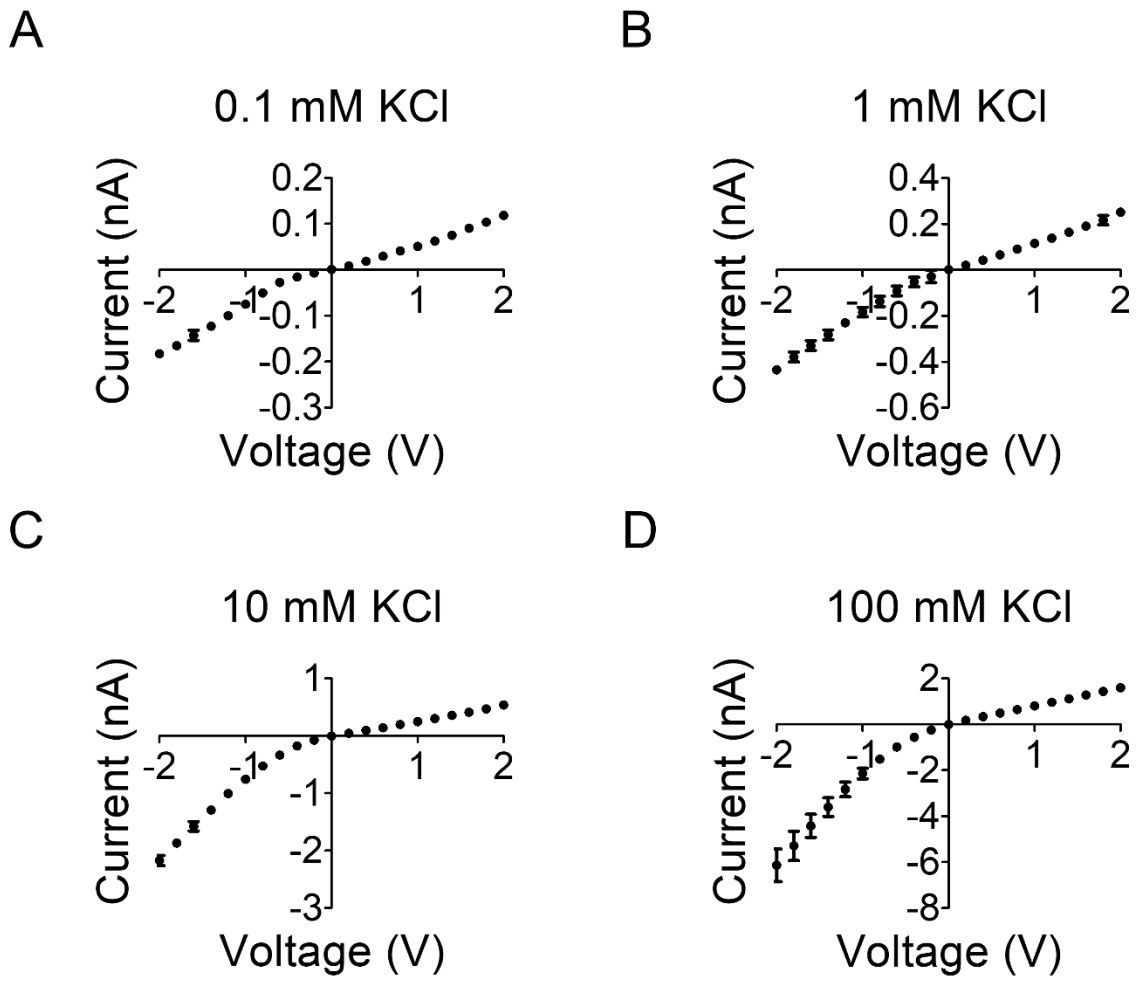

Figure 5.2. Current-voltage curves of a single as prepared conical nanopore with a tip opening of 14 nm and a base opening diameter of 640 nm recorded in various

concentrations of KCl as indicated in the figure. All current-voltage curves are averages of three forward and reverse scans.

Figure 5.3 shows i-V curves for the same 14 nm conically shaped pore modified with PAH and recorded at various concentrations of KCl. As expected, all the i-V curves were reversed such that with the same electrode configuration, the positive ion currents are greater than negative ion currents.

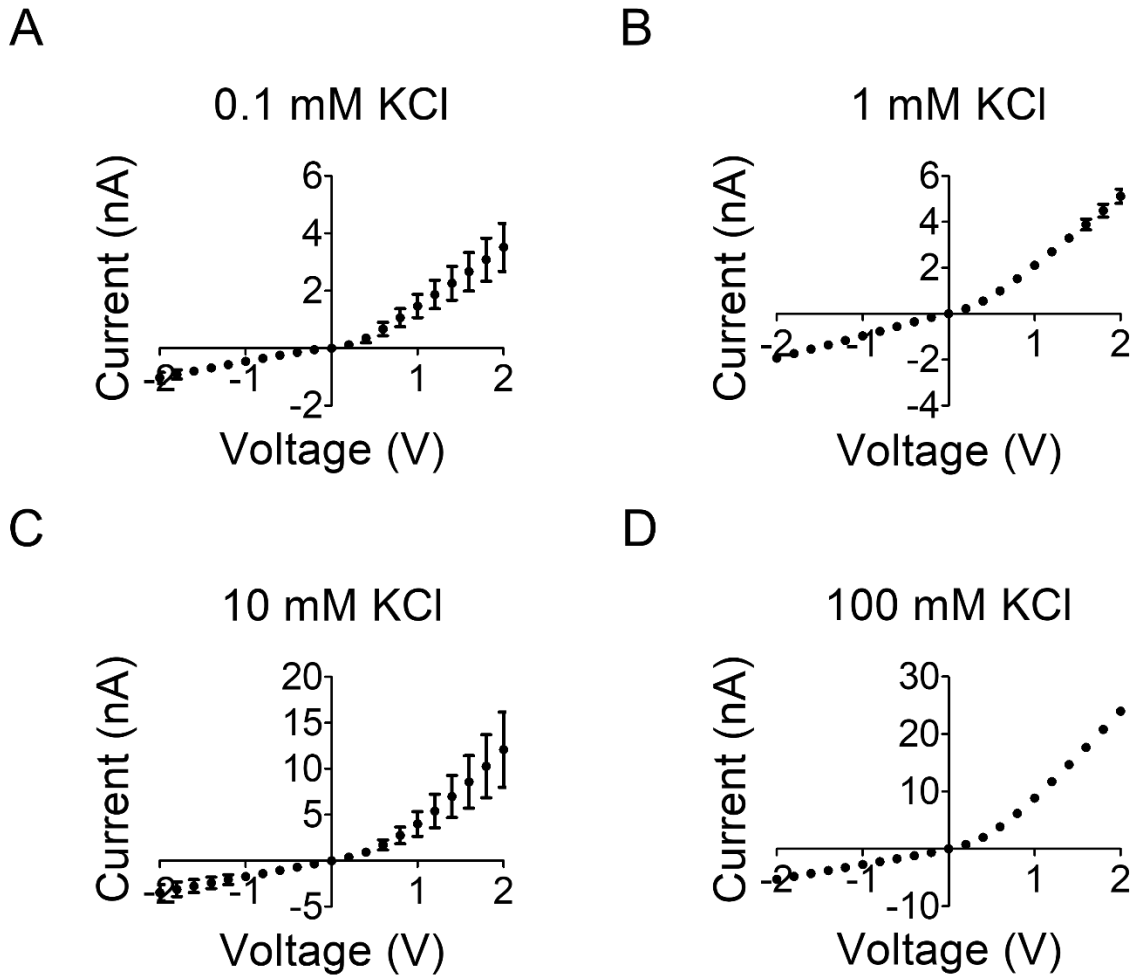

Figure 5.3. Current-voltage curves of a single conical nanopore modified with PAH with a tip opening of 14 nm and a base opening diameter of 640 nm recorded in various concentrations of KCl as indicated in the figure (the same nanopore as in Figure 2). All current-voltage curves are averages of three forward and reverse scans.

5.2. Studying charge inversion of nanoconfined single conical pores in trivalent tris(ethylenediamine)chromium(iii) sulfate electrolyte solutions

Next, as prepared track-etched single conically shaped PET nanopores were exposed to a set of tris(ethylenediamine)chromium(iii) sulfate salt solutions. The i-V curves were recorded in the voltage ranges between - 2 V and + 2 V. For the purposes of this manuscript and all theoretical calculations here forth, we assume the diameter of tris(ethylenediamine)chromium(iii) to be the same as cobalt(III) sepulchrate chloride (CoSep) used in our earlier experiments: 0.89 nm.[12]

The main questions we wanted to address with this work are as following. How does charge inversion influence the conductance of conically shaped nanopores with small tip diameters between in tens of nanometers? More specifically, is it possible that when the pore diameter is less than 10 nm, the accumulation of trivalent ions in the pore is hindered such that charge inversion is prevented? In this regime, is the volume of the conically shaped nanopore unable to be filled with a high concentration of bulky Cr^{3+} and SO_4^{2-} ions? Does the accumulation of the bulky ions lead to current blockage? And lastly, does the extreme nano-confined geometry of the conically shaped pore interfere with and prevent charge inversion from happening?

For charge inversion to occur, a certain concentration threshold of multivalent ions in the bulk solution must be met and the potential of the Stern layer, must overcompensate the potential of the bare surface charge density. This concentration threshold, c_0, can be calculated using the following equation:[99]

$$c_0 = \left|\frac{\sigma_b}{2r_{ion}Ze}\right| e^{\frac{\mu_c}{kT}} \qquad \text{eq. (5.1)}$$

where: r_{ion} is the ionic radius, σ_b, the bare pore surface charge density, Z, the ion valency, e is the elementary charge of an electron, k_B, the Boltzmann constant, T is temperature, and μ_c, the chemical potential that accounts for the spatial interactions between multivalent ions in the Stern layer. The chemical potential is equal to:

$$\mu_c = -k_B T(1.65\Gamma - 2.61\Gamma^{\frac{1}{4}} + 0.26ln\Gamma + 1.95) \qquad \text{eq. (5.2)}$$

where Γ, also commonly referred to as the Coulomb coupling constant, is the interaction parameter between the multivalent ions in the Stern layer and is defined as:

$$\Gamma = \frac{1}{4k_B T \varepsilon_0 \varepsilon_r} \sqrt{\left|\frac{e^3 Z^3 \sigma_b}{\pi}\right|} \qquad \text{eq. (5.3)}$$

where ε_r is the dielectric constant and ε_0, the permittivity of free space.

In addition to $c_{bulk} > c_0$ ($|\sigma_{Stern}| > |\sigma_b|$), Γ ≥ 1 for charge inversion to occur and is typically achieved when Z ≥ 2. For example, in KCl, Γ = 0.9 compared to tris(ethylenediamine)chromium(iii) sulfate where Γ = 4.6.[103] This makes KCl and other similar monovalent electrolytes at room temperature, unable to form spatial correlations and undergo charge inversion. This theoretical calculation is also consistent with experimental data where charge inversion has not been reported in KCl. Furthermore, previous reports point to the use of divalent (Z = 2) and trivalent (Z = 3) salts to investigate charge inversion.[12] However, in the case of salts with divalent or trivalent cations, if $c_{bulk} < c_0$ ($|\sigma_{Stern}| < |\sigma_b|$), the effective surface charge of the pore walls will remain negative. Increasing c_{bulk} (= c_0) does lead to the effective surface charge being neutralized ($|\sigma_{Stern}| = |\sigma_b|$), and eventually, over screened ($c_{bulk} > c_0$) which is when the effective surface charge of the pore walls switches sign (Figure 5.4), and the measured i-V curve is completely inverted.

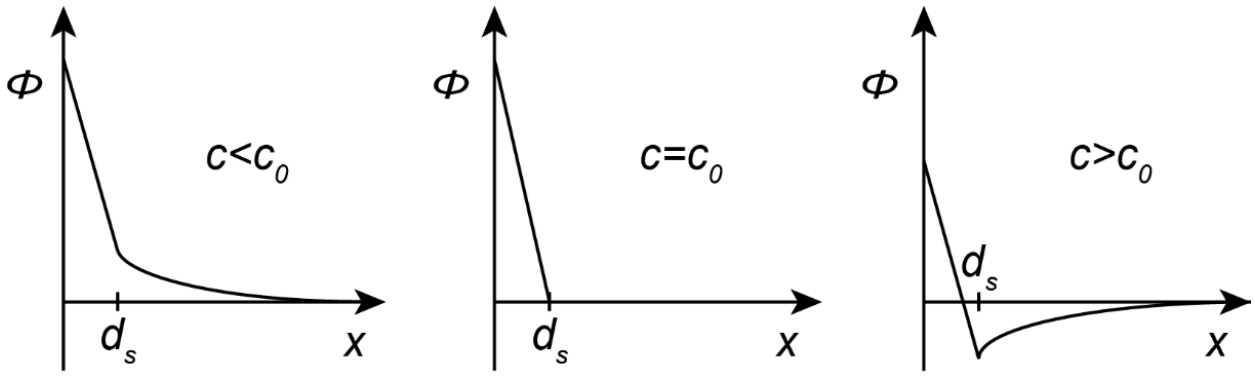

Figure 5.4. Sketch of the electrostatic potential φ as a function of the distance x from a surface with constant σ_b for the cases: $c < c_0$ (no charge inversion), $c = c_0$ (neutralization of the surface charge), and $c > c_0$ (charge inversion). Here, d_s is the distance of the Stern layer.

The reason why the effective surface charge changes from negative to positive is because of the strongly correlated liquid that's formed by divalent or trivalent cations at the negatively charged interface of the as prepared pore walls. In the strongly correlated liquid model, positions of cations at the pore surface are laterally correlated in such a manner that they create a structure that resembles a Wigner crystal of electrons. The organization of the multivalent cations lowers the potential energy of the system, overcomes their electrostatic repulsion, and makes charge inversion thermodynamically favorable.

Utilizing equation 5.1, we predict the minimum threshold concentration needed to induce charge inversion and onset the reversal of the surface charge density (c_0) to be 0.6 mM tris(ethylenediamine)chromium(iii) sulfate assuming σ_b is equal to |-80| mC/m^2. Figure 5.5 shows i-V curves and current-time series of a single conically shaped nanopore with a 25 nm small opening diameter recorded in various concentrations of tris(ethylenediamine)chromium(iii) sulfate. All i-V curves were obtained by averaging the current-time series signals. At 0.1 mM tris(ethylenediamine)chromium(iii) sulfate, the nanopore behaves like an ohmic resistor exhibiting a linear i-V curve (Figure 5.5 A). This recording suggests that the effective surface charge is neutralized even though, 0.1 mM is below the concentration threshold needed to induce charge inversion. This means that at these experimental conditions, the pore walls are still expected to be negatively charged. The linear i-V curve, however, originates from the voltage enhanced concentration of cations in volume of the conically shaped nanopore. Therefore, the pore walls are in contact with an effectively greater concentration of cations than 0.1 mM. It is noted though, that at 0.1 mM, the pore conductance (blue curve in Figure 5.5 A) is very similar to the value calculated based on the bulk conductivity of the tris(ethylenediamine)chromium(iii) sulfate salt and the pore geometry. This result indicates that the correlated Cr^{3+} ions do not induce any steric effects on the measured current.

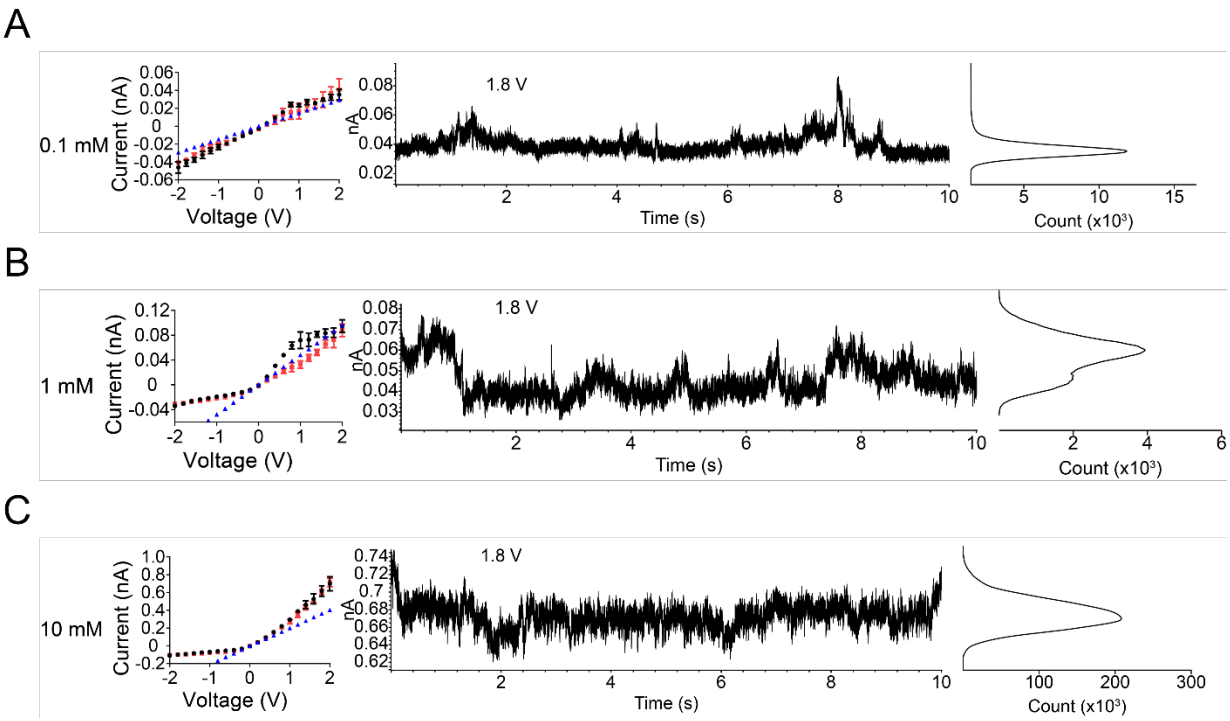

Figure 5.5. Current-voltage curves and current-time series (1.8 V) of a single conically shaped nanopore with a tip opening of 25 nm recorded in various concentrations of tris(ethylenediamine)chromium(iii) sulfate as indicated in the figure. The recordings were performed at pH 8 with symmetric concentrations of tris(ethylenediamine)chromium(iii) sulfate on both sides of the conductivity cell. The base opening of this pore was 680 nm. Histograms of the ion current values are shown to the right. The currents in blue correspond to calculated values assuming the pore is filled with the bulk solution of 0.1 mM, 1 mM, and 10 mM Cr^{3+} respectively.

When the bulk concentration of tris(ethylenediamine)chromium(iii) sulfate reaches 1 mM, the directionality of the i-V curve is inverted (Figure 5.5 B), compared to KCl in a negatively charged as prepared pore (Figure 5.1 C), suggesting that the pore walls became effectively positively charged, and the pore is now anion selective. The existence of the effective positive surface charge at this concentration agrees with the theoretical prediction that charge inversion is expected to occur when the bulk concentrations reach 0.6 mM. The i-V curve also has the same direction of rectification as the recording obtained using symmetric concentrations of KCl for a positively charged pore modified with PAH (Figure 5.1 D). These findings are in agreement with previous experimental

results showing the switching of the selectivity and surface charge polarity (from negative to positive) of silicon dioxide nanochannels and PET nanopores using another trivalent cation, CoSep.[12,100] This further illustrates the consistency between the experimentally obtained, multivalent data and the theoretical strongly correlated liquid model.

It is at 1 mM tris(ethylenediamine)chromium(iii) sulfate however, that we start to see some additional transport properties, such as hysteresis and ion current instabilities. The hysteresis in Figure 5.5 B is especially pronounced at positive potentials above 1 V. As the voltage is scanned in the forward direction, from - 2 V to + 2 V, the positive currents are larger in magnitude than when the voltage is scanned in the opposite direction from + 2 V to - 2 V. The ion currents at high positive voltages exhibited fluctuations in time. It is also noted, that when the tris(ethylenediamine)chromium(iii) sulfate concentration increases from 0.1 to 1 mM, the current at positive voltages increased by a factor of two, and the currents at negative voltages, remain unchanged. Although the pore resistance for positive voltages is nonlinear for the forward direction, the average current is close to the value calculated based on the bulk conductivity (blue curve in Figure 5.5 B). The values of negative currents conversely, are much lower than expected. As the concentration of tris(ethylenediamine)chromium(iii) sulfate is increased to 10 mM, the way in which the ion current rectifies becomes more pronounced, and the positive ion current again increases nonlinearly with the increasing voltage for both the forward and reverse scans. At this concentration, the positive currents are much higher than what is predicted based on the bulk conductivity. This suggests that the higher concentration of Cr^{3+} ions lead to a higher effective positive, surface charge density on the pore walls, an accumulation of accumulations of mobile SO_4^{2-} ions, and an enhanced ion conductance.

The 25 nm nanopore is sufficiently large enough that the finite size of the Cr^{3+} and SO_4^{2-} ions do not need to be considered to explain the i-V measurements. However, smaller nanopores will be probed and the recorded ion current will be influenced by two opposite effects. The first being correlated Cr^{3+} ions that can lead to steric hindrance such that their layer effectively diminishes the small tip opening pore diameter. The second, is the increase of the local positive charge as more Cr^{3+} get adsorbed, leading to the accumulation of negative SO_4^{2-} and a higher overall conductance. It is noted that these

two effects become more evident as the applied voltage increases. The increased ion current instabilities at the higher positive voltages in 1 mM and 10 mM tris(ethylenediamine)chromium(iii) sulfate might, we believe, stem from the steric effects of the accumulated ions, as we will discuss in more detail below.

Figure 5.6 shows i-V curves and examples of the ion current in time signals for a conically shaped nanopore that has 10 nm tip opening diameter. This pore exhibits charge inversion at the lowest probed concentration, 0.1 mM tris(ethylenediamine)chromium(iii) sulfate, a concentration that is six times lower than the value predicted by eq. 5.1.

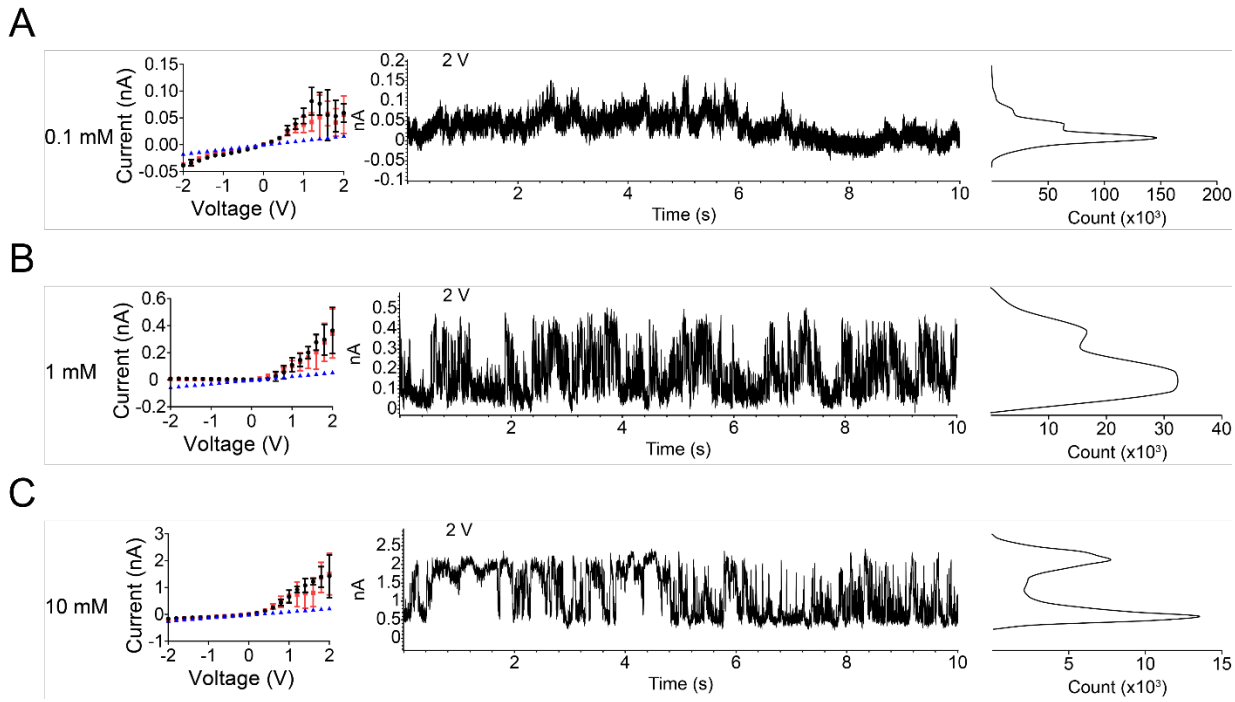

Figure 5.6. Current-voltage curves and current-time series (2 V) of a single conically shaped nanopore with a tip opening of 10 nm recorded in various concentrations of tris(ethylenediamine)chromium(iii) sulfate as indicated in the figure. The base opening of this pore was 1 μm. Histograms of the ion current values are shown to the right. The currents in blue correspond to calculated values assuming the pore is filled with the bulk solution of 0.1 mM, 1 mM, and 10 mM Cr^{3+} respectively.

As the concentration increases to 1 and 10 mM, the ion current rectification becomes more pronounced. Interestingly, the average currents for the positive voltages at all the

examined concentrations are greater than all the values calculated based on bulk conductivity, suggesting that the enhanced local concentration of ions, and not the steric effects, dominated the transport properties of the nanopore. Smaller conical nanopores, induce a greater enhancement of the local ionic concentration at positive voltages than a wider, much larger nanopore.[123] Consequently, positive currents in the 10 nm pore are more pronounced than positive currents in the 25 nm nanopore.

This pore, however, exhibited significant fluctuations of the ion current in time. At 1 mM and 10 mM, the pore switched between being closed to a finite set of open state values (Figure 5.6 B & C). We postulate that the ion current fluctuations originate from the voltage-dependent accumulation of Cr^{3+} ions in the volume of the pore, and the voltage dependent surface charge density caused by the correlated ions. We hypothesize that once the correlated ions reach a maximum surface density, the correlated liquid structure becomes unstable and is released from the surface, allowing the Cr^{3+} accumulation to re-start. We believe that the ion current fluctuations can be explained the following way: As the density of correlated Cr^{3+} ions on the surface increases, the current increases due to the rise of mobile SO_4^{2-} ions. The release of the unstable correlated liquid structure conversely, will be observed as an instantaneous decrease of the ion current.

Figure 5.7 shows the transport properties of a 6 nm in diameter conically shaped nanopore. Analysis of the i-V curves suggests that the enhancement of the ion current at positive voltages in 0.1 mM and 1 mM tris(ethylenediamine)chromium(iii) sulfate is weaker than what we saw in the 10 nm pore, and at 10 mM tris(ethylenediamine)chromium(iii) sulfate charge inversion was no longer observed. These recordings indicate that we start to observe the effect of steric hindrance in the i-V curves. The steric hindrance can cause a decreased density of correlated Cr^{3+} ions on the surface and a decrease of the effective opening diameter of the pore that the Cr^3 ions cause. In 0.1 mM tris(ethylenediamine)chromium(iii) sulfate, there also seems to be a threshold for the positive voltages' ability to transport ions in the forward bias direction together with a strong hysteresis.

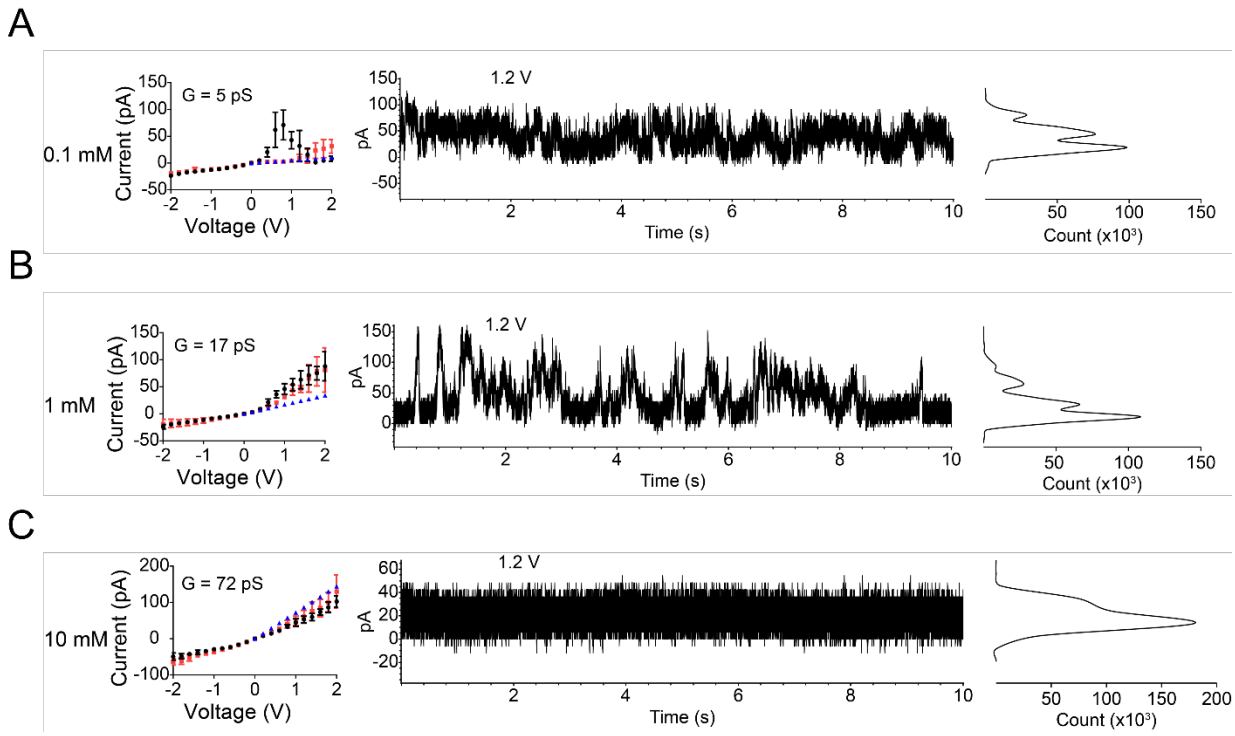

Figure 5.7. Current-voltage curves and current-time series (1.2 V) of a single conically shaped nanopore with a tip opening of 6 nm recorded in various concentrations of tris(ethylenediamine)chromium(iii) sulfate as indicated in the figure. The base opening of this pore was 1040 nm. Histograms of the ion current values are shown to the right. The currents in blue correspond to calculated values assuming the pore is filled with the bulk solution of 0.1 mM, 1 mM, and 10 mM Cr^{3+} respectively.

This phenomenon of prohibited current flow under extreme confinement is further exemplified with the 4 nm pore. Particularly, when the nanopore was sampled at 0.1 mM tris(ethylenediamine)chromium(iii) sulfate where it exhibited a conductance that is again less than what is expected from bulk conductivity and the current-voltage curves are linear (Figure 5.8 A). Increasing the bulk concentration to 1 mM tris(ethylenediamine)chromium(iii) sulfate did not lead to an increased current (Figure 5.8 B). The most surprising observation from this pore was the lack of charge inversion even at 10 mM, where the nanopore rectifies as if the pore is still negatively charged (Figure 5.8 C). This suggests that when the pore diameter is less than 5 nm, the local Cr^{3+} concentration and effective surface charge might be a strong function of the pore opening diameter.

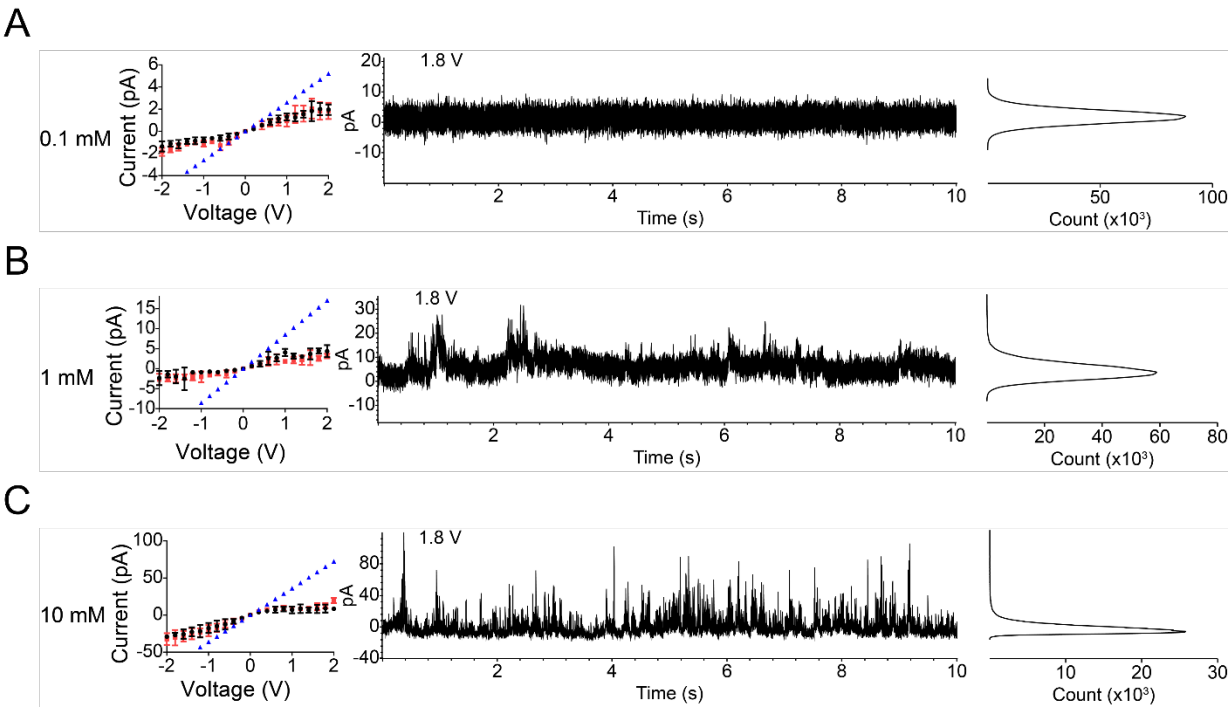

Figure 5.8. Current-voltage curves and current-time series (1.8 V) of a single conically shaped nanopore with a tip opening of 4 nm recorded in various concentrations of tris(ethylenediamine)chromium(iii) sulfate as indicated in the figure. The base opening of this pore was 720 nm. Histograms of the ion current values are shown to the right The currents in blue correspond to values calculated assuming the pore is filled with the bulk solution of 0.1 mM, 1 mM, and 10 mM Cr^{3+}, respectively.

Chapter 6.

Solid-Liquid Interfaces in Organic Solvents: Enhanced Electroosmosis in Propylene Carbonate Salt Solutions

A pore with excess surface charges placed in a salt concentration gradient will induce electroosmotic flow: for one voltage polarity the pore will be filled with the more concentrated solution and for the opposite polarity, the less concentrated solution.[81] Such pore exhibits conductance that is dependent on the polarity of the applied voltage the surface charges of the pore walls, and ultimately, rectifies the ion current. Much like our earlier findings[41], the PET pores reported here are shown to switch their surface potential from negative in an aqueous $LiClO_4$ concentration gradient to positive in a propylene carbonate salt concentration gradient. To further quantify the negative surface potential/charge in water, and the positive surface potential/charge in propylene carbonate, we utilized the resistive-pulse technique. Using largely uncharged polystyrene particles as a probe, we measured their electroosmotic velocity in single PET pores in water and propylene carbonate as a function of applied voltage.[37] These measurements allowed us to determine the polarity of the surface potential of the pore walls and estimate the zeta potential of the polymer wall/solution (solid-liquid) interface. Our results revealed that in propylene carbonate solutions, the electroosmotic transport was not only reversed, but also significantly enhanced compared to the recordings in water.

6.1. Current-voltage measurements in aqueous and propylene carbonate $LiClO_4$ solutions

When a cylindrical pore with as prepared, negative or PAH modified, positive surface charges is placed in contact with two solutions of differing concentrations and thus, differing conductivities, the recorded i-V curves rectify. Ion current rectification here, stems from electroosmosis that depending on the voltage polarity, fills the pore with a solution of higher or lower conductivity.[37,41,81] Pores with negative surface charges and pores with positive surface charges on the walls are expected to exhibit distinct current-voltage curves that are symmetric with respect to the origin of the coordinate system (Figure 6.1). Figure 6.1 shows i-V curves of a single 660 nm cylindrical PET pore placed in contact with a 20 mM and 200 mM concentration gradient of $LiClO_4$. These initial

measurements were performed with $LiClO_4$ due to the salt being soluble in a variety of different solvents.

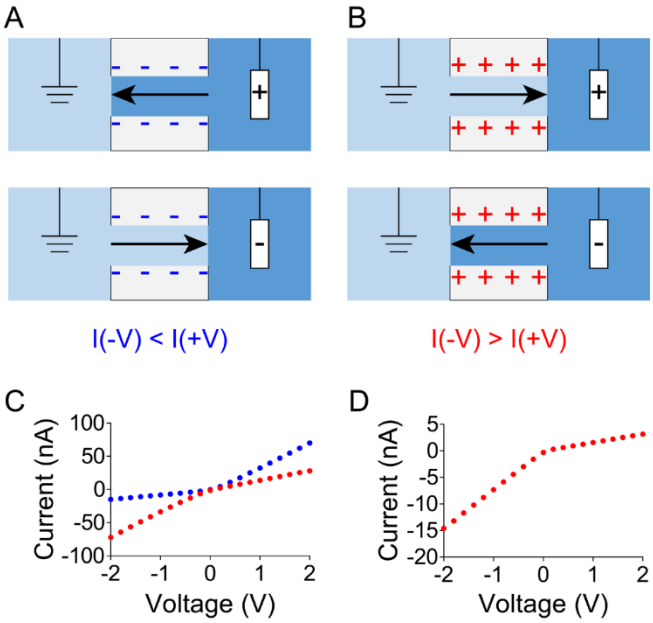

Figure 6.1. Probing surface charges in a single pore by measuring the current-voltage curves in a salt concentration gradient. A pore is placed in a conductivity cell whose chambers are filled with solutions of $LiClO_4$ but at different concentrations, in this case 20 mM and 200 mM. (A, B) Schemes showing ion concentration in the pore as a function of polarity, applied voltage and the surface charge. The darker blue color indicates 200 mM $LiClO_4$ and the lighter blue, 20 mM $LiClO_4$. The arrows indicate the direction of electroosmosis. (A) If a pore carries negative surface charges, the direction of electroosmosis is determined by the direction of cation migration. At positive voltages, cations move from the chamber with 200 mM $LiClO_4$ and electroosmotically drags the solution into the pore. Conversely, at negative voltages, cations are sourced from 20 mM $LiClO_4$, and the pore will be filled with the less concentrated solution. This pore will rectify the current such that positive currents are larger than negative currents. (B) A pore with positive surface charges will be filled 20 mM (200 mM) $LiClO_4$ at positive (negative) voltages. This pore will exhibit higher currents at negative voltages than positive voltages. The direction of eletroosmosis in this pore is determined by the migration of anions. (C) Recordings for a 660 nm diameter PET pore placed in a concentration gradient of 20 and 200 mM $LiClO_4$ solutions of water. The blue curve was obtained for the pore as prepared,

while the red curve was recorded after the pore had been modified with PAH that rendered the surface charge positive. (D) Recordings for the same 660 nm pore as prepared in a propylene carbonate 20 and 200 mM $LiClO_4$ concentration gradient. All current-voltage curves are averages of three scans.

For an unmodified pore in contact with aqueous solutions, when the working electrode is placed into the solution of higher conductivity (200 mM $LiClO_4$), and the ground electrode into the solution of lower conductivity (20 mM $LiClO_4$), cationic (Li^+) current will electroosmotically fill the pore with the 200 mM $LiClO_4$ solution at positive potentials and with the 20 mM solution at negative potentials (Figure 6.1 A). The measured ion current is directly proportional to the solution conductivity and number of charge carriers in the pore.[86] Therefore, a pore as prepared in aqueous solutions will exhibit an ion current rectification wherein currents at positive voltages are greater than currents at negative voltages (Figure 6.1 A and the blue recording in Figure 6.1 C). Conversely, after PAH modification, anionic (ClO_4^-) current electroosmotically fills the pore with the solution of higher conductivity at negative potentials, and the solution of lower conductivity at positive potentials (Figure 6.1 B). Therefore, a pore with a positive surface charge exhibits larger currents at negative voltages than at positive voltages (Figure 6.1 B and the red recording in Figure 6.1 C). The experiments performed in Figure 6.1 C exemplify how the polarity of the surface potential this time, of a cylindrically shaped PET pore can be deduced from the direction of rectification observed in experimentally obtained i-V curves recorded with the salt electrolyte concentration gradient.

The same unmodified pore as shown in Figure 6.1 C was also tested using a 20- and 200-mM concentration gradient of $LiClO_4$ in propylene carbonate. The i-V curve of the as prepared pore in propylene carbonate solutions of $LiClO_4$ (Figure 6.1 D) has the same direction of rectification as the i-V curve of the positively charged pore probed using the aqueous salt concentration gradient (red curve in Figure 6.1 C). These recordings suggest that the same pore that was negatively charged in water, became positively charged in the organic solvent. These findings agree with our previous results showing the positive surface charge of PET[41] and polycarbonate pores in propylene carbonate salt solutions.[25]

The method of probing the surface charge polarity via ion current rectification and salt concentration gradients is applicable to pores of any size and/or shape. However, it does not provide any quantitative information on the surface charge density or magnitude of the surface potential. To compare the electrochemical properties of the PET-liquid interface in water and propylene carbonate, we performed resistive-pulse experiments where individual polystyrene particles were electrokinetically transported through a single PET pore.

6.2. Resistive-pulse measurements in aqueous $LiClO_4$ solutions

In the resistive-pulse sensing, transmembrane electric potential (or pressure difference) causes the passage of individual objects through a pore that is detected as a transient change of the transmembrane current, called a pulse or event.[128] The amplitude, duration as well as local ion current characteristics of each pulse affords information about the physical and chemical properties of the analyte.[80,129,130] However, in situations where the analyte is known, e.g., when a particle is of known size and shape, the recorded current resistive-pulse events can be used to inform us about the geometry of the pore used in the experiments. The shape of the ion current pulses reveals e.g., the conical shape of a pore[72,131], or the existence of local inhomogeneities in the pore opening.[80,132,133]

Resistive-pulse measurements were initially performed in water to characterize and verify that the direction of electroosmotic translocation agreed with the surface charge of the PET pores. Experiments were performed with as prepared, single PET pores with negative surface charges and pores subjected to PAH modification (Figure 6.2 A, B). We began experimenting with aqueous KCl solutions since resistive-pulse measurements in this electrolyte are best understood and characterized.[71,129,134–136] In our first experiment, we used unfunctionalized i.e., mostly uncharged, 400 nm polystyrene beads suspended in 100 mM KCl and 0.001 % v/v TWEEN 20. The concentration of the particles was ~10^9 particles/mL. The particles are largely uncharged as elucidated from their low, few mV magnitude zeta (ζ) potential.[137] The particle suspension was placed on one side of the conductivity cell with the ground electrode. The other side of the pore was in contact with the same salt/TWEEN solution without particles (Figure 6.2 A, B).

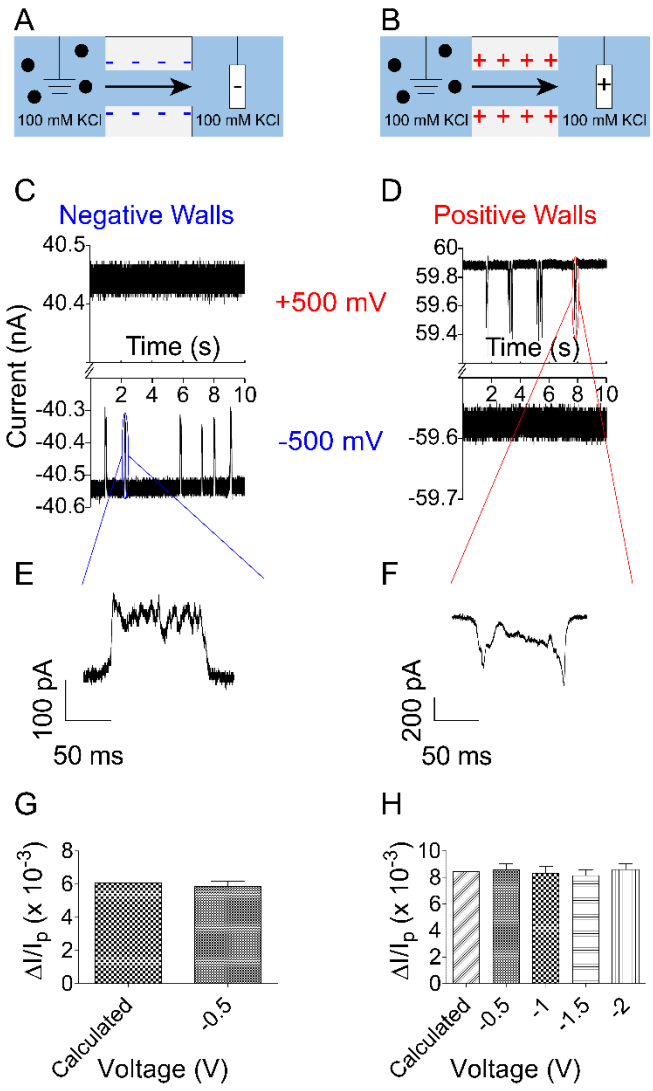

Figure 6.2. Resistive-pulse experiments in 100 mM aqueous solution of KCl using 400 nm diameter unfunctionalized polystyrene particles. Measurements were performed with single cylindrically shaped PET pores with a negative surface charge (A), and a positive surface charge when modified with PAH (B). (A, B) The direction of electroosmotic flow is marked with an arrow for the voltage polarity that is expected to bring the solution containing particles into the pore. (C) Measurements of the ion current in time series through an as prepared 1 μm diameter PET pore at +/- 500 mV. This pore was negatively charged. (D) Ion current time series for a 1.2 μm diameter pore modified with PAH at +/- 500 mV. (E, F) Example shapes of ion current pulses. (G) Analysis of the pulses for the recordings shown in the panel (C). (H) Analysis of pulses through a different pore with an

opening diameter of 870 nm used to electroosmotically translocate 400 nm diameter particles at different transmembrane potentials. This pore was negatively charged.

Figure 6.2 C shows ion current signals in time recorded with a pore as prepared that had an effective opening diameter of 1 μm. Recordings with another pore with an effective opening diameter of 1.2 μm that had been modified with PAH is also shown in Figure 6.2 D. Both pores were tested at +/- 500 mV. Distinct ion current pulses were observed for the negatively charged pore only at negative transmembrane potentials and for the positively charged pore, at positive voltages. The particles only translocated through the pores for the voltage polarities that electroosmotically brought the solution with particles into the pores (Figure 6.2 A, B). The direction of electroosmotic translocation agrees with the surface charge of the pores' walls. By which, a pore with a negative (positive) surface charge exhibits particle translocation in the direction determined by cation (anion) flow. The absence of measurable ion current pulses in the opposite (electrophoretic) direction further validates the notion that the polystyrene particles used throughout experimentation were largely uncharged. Figure 6.2 E & F shows examples of zoomed in ion current pulses recorded for the two examined pores using the 400 nm particles. The presence of current undulations within each pulse agrees with earlier reports showing the pores exhibiting an undulating diameter along the axis.[80,132] The repeatable signature of the current pulses also allows us to confirm that the pulses correspond to the particles' complete translocation, and not approaches to the pore opening without successful passages.

The relative amplitude of the ion current pulses, $\Delta I/I_p$, is known to be a function of the particle, d, and the pore, D, diameters:[71,128]

$$\frac{R_p - R_e}{R_e} = \frac{I_e - I_p}{I_p} = \frac{d^3}{D^2(L+0.8D)}\, S\left(\frac{d}{D}\right) \qquad \text{eq. (6.1)}$$

where: R_p and R_e (I_p and I_e), indicate the electrical resistance (ion current) of the system with and without a particle in the pore, respectively, and L is the pore length. The expression 0.8D accounts for the access resistance of the pore.[112,113,138] The proportionality coefficient, $S\left(\frac{d}{D}\right)$, is the so-called shape factor and has the following form:[128]

$$S\left(\frac{d}{D}\right) = \left[1 - 0.8\left(\frac{d}{D}\right)^3\right]^{-1} \qquad \text{eq. (6.2)}$$

Figure 6.2 G & H shows the analysis of the relative current decrease (the events) associated with the passage of the 400 nm particles through the negatively charged single pores. The magnitude of the experimentally observed current change, $\Delta I/I_p$, correlates very well with the magnitude predicted by eq. (6.1) at all the examined voltages suggesting that the particles do translocate individually and do not undergo aggregation.

Resistive-pulse experiments were also performed in an aqueous solution of $LiClO_4$, the salt used in the propylene carbonate experiments. Figure 6.3 A-D shows examples of pulses obtained in 100 mM $LiClO_4$ and compares them with recordings in 100 mM KCl for the same pore. The passage of particles only occurred at negative voltages in KCl and $LiClO_4$. This confirms that the pore was negatively charged in the presence of K^+ and Li^+. At negative voltages, our electrode configuration sources cations from the side of the pore that contains the particle suspension, enabling particle passage. The amplitude of the ion current pulses in both salts correlated well with one another. Example ion current pulses shown in Figure 6.3 C & D indicate that the passage velocities of the particles in KCl and $LiClO_4$ are similar further suggesting that the PET-liquid interface in these two salts are comparable. The event duration time is analyzed in detail below.

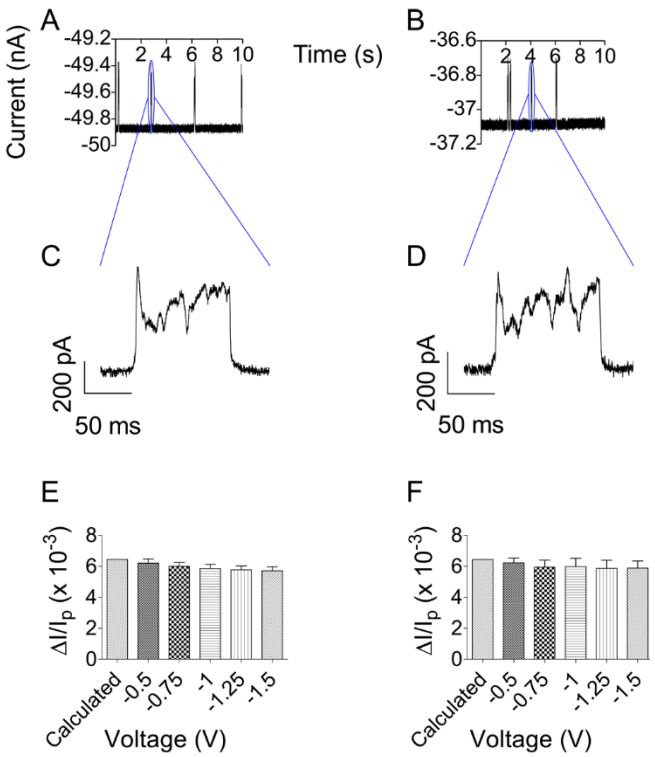

Figure 6.3. Transport of 400 nm polystyrene particles in aqueous solutions of 100 mM KCl (left panels) and 100 mM $LiClO_4$ (right panels). All measurements were performed with an 860 nm diameter pore. (A, B) Ion current signal in time at -750 mV with events indicating translocating particles. (C, D) Example zoomed-in ion current pulses. (E, F) Analysis of pulses shown in (A, B), together with the theoretical value calculated based on eq. (6.1).

6.3. Resistive-pulse measurements in propylene carbonate $LiClO_4$ solutions

Resistive-pulse measurements were also performed in a 200 mM $LiClO_4$ solution in propylene carbonate to further probe how the organic solvent affects the surface charge of the PET pores, and to substantiate the results obtained in Figure 6.1. With a similar experimental set-up as used with the aqueous solutions (Figures 6.2 & 6.3), 400 nm polystyrene particles were suspended in a 200 mM $LiClO_4$ propylene carbonate solution with 0.05 % v/v TWEEN 80. We used 200 mM ($LiClO_4$) as the concentration of the background electrolyte due to the significantly reduced conductivity of propylene carbonate salt solutions. The increased salt concentration (compared to 100 mM KCl in

water) allowed us to increase the signal of the ion current and the current change due to particle translocation.

To probe the surface charge of an as prepared PET pore in the propylene carbonate $LiClO_4$ solution, the suspension containing the uncharged 400 nm diameter polystyrene particles were once again placed into the chamber of the conductivity cell containing the ground electrode (Figure 6.4 A). This allowed the surface charge of the PET pore to be elucidated from the directionality of electroosmotic translocation of the particles. Figure 6.4 B shows ion current recordings observed at positive and negative voltages (+/- 1 V). The measurements revealed that the particles translocated through the pore only at positive voltages. This suggests that the surface charge of the PET pore became positive since positive voltages can bring the particles into the pore only if the direction of electroosmotic flow is determined by negative ions, much like the recordings in Figure 6.2 D. The results shown in Figure 6.4 also indicate a larger variability of the pulse amplitude compared to the recordings in water. The 1 μm pore used in these experiments is the same pore as in Figure 6.2 C, E & G. The similar shapes of the ion current pulses in aqueous (Figure 6.2 E) and propylene carbonate (Figure 6.4 C) based solutions also suggests that the particles successfully translocated in both media.

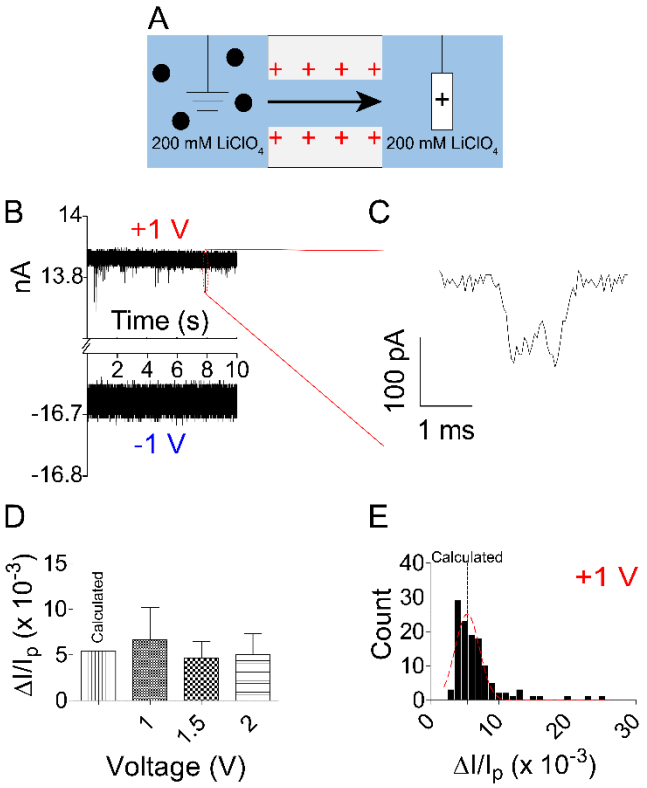

Figure 6.4. Resistive-pulse experiments with 400 nm particles in a 200 mM solution of $LiClO_4$ in propylene carbonate. (A) Measurements were performed with an unmodified, as prepared, 1 µm diameter PET pore and particles present in only one chamber of the conductivity cell. The experiments point to the presence of a positive surface charge on the pore walls. (B) Ion current time series recorded at +/- 1 V and the respective magnified resistive-pulse event (C). (D) Average amplitude of ion current pulses at different voltages. (E) Example histogram of $\Delta I/I_p$ at 1 V. The pore used in these experiments is the same as the pore shown in Figure 6.2 C.

Recordings of the ion current in propylene carbonate were subjected to a similar analysis as performed in Figure 6.2 G & H. Figure 6.4 D shows that the average amplitude of the ion current pulses at the three magnitudes of applied voltage is consistent with the predicted $\Delta I/I_p$. However, histograms of the experimentally measured amplitude of the events (Figure 6.4 E at 1 V) reveal the presence of $\Delta I/I_p$ values that are twice the theoretical prediction. These large values of $\Delta I/I_p$ suggest that the particles might have undergone aggregation in propylene carbonate.

The hypothesis of the particles aggregating in solution is also supported by the observation that their translocations would typically be recorded within the first ~20 minutes of introducing the particles into the solution. Moreover, DLS experiments performed with suspensions of these particles in 200 mM LiClO4 propylene carbonate did not yield any tangible results concerning the particles' size due to the large polydispersity index (≥ ~0.3) that increased with the measurement time.

Lastly, we confirmed that exposure of PET pores to propylene carbonate-based solutions did not change the effective pore opening. Current-voltage curves of an 860 nm diameter pore in 1 M KCl before and after exposing it to a 200 mM LiClO4 propylene carbonate solution with 0.05 % v/v TWEEN 80 are nearly identical to one another. This suggests that the pore did not undergo swelling or any other changes that would alter its effective opening. We would also like to note that the average $\Delta I/I_p$ recorded in propylene carbonate agrees well with the theoretically predicted value, providing evidence that the particles did not undergo swelling in the organic solution either.

6.4. Quantification of the zeta potential in aqueous and propylene carbonate $LiClO_4$ solutions

The voltage polarity at which the particles translocate through the pore informs us about the polarity of the surface charges on the pore walls. In a negatively (positively) charged pore, the particles are transported in the direction of electroosmotic flow as determined by the cations (anions) in solution. To quantify the magnitude of the surface potential, we analyzed in detail the duration of the ion current pulses, which is a measure of the particles' translocation velocity. From the Einstein-Smoluchowski equation, the velocity of each resistive-pulse event can be related to the zeta (ζ) potential of the pore walls through the following relation:[37]

$$\nu_{EOF} = \frac{\varepsilon_0 \varepsilon_r \zeta_{Pore} E}{\eta} \qquad \text{eq. (6.3)}$$

where: v_{EOF} is the electroosmotic velocity of the particles, ε_0, the permittivity of free space, ε_r is the dielectric constant, ζ_{Pore}, the zeta potential of the pore wall, E is the electric field strength, and η, the solution viscosity. Equation (6.3) assumes that the particles are uncharged. Note that ζ_{Pore} is the potential at the shear plane. The value of ζ_{Pore} is expected

to be less than the electric potential at the surface.[38] Acknowledging that, $v_{EOF} = \frac{L}{t}$ where: t is the resistive-pulse event duration time, and knowing that $E = \frac{V}{L}$[117], one obtains:

$$\frac{L}{t} = \frac{\varepsilon_0 \varepsilon_r \zeta_{Pore} V}{\eta L} \qquad \text{eq. (6.4)}$$

Rearranging equation 6.4 allows one to plot the duration of resistive pulses as a function of the inverse applied voltage:[130]

$$t = \frac{\eta L^2}{\varepsilon_0 \varepsilon_r \zeta_{Pore} V} \qquad \text{eq. (6.5)}$$

Figure 6.5 A shows the event duration time measured in 100 mM aqueous $LiClO_4$ using the same pore as shown in Figure 6.3. The magnitude of ζ_{Pore} for the PET pore walls in the aqueous solution was calculated to be -4 ± 1 mV. This value agrees with earlier reports on the decreased zeta potential in concentrated salt solutions.[37,139] The measured ζ_{Pore} in 100 mM KCl for the same pore was also ~ -4 mV.

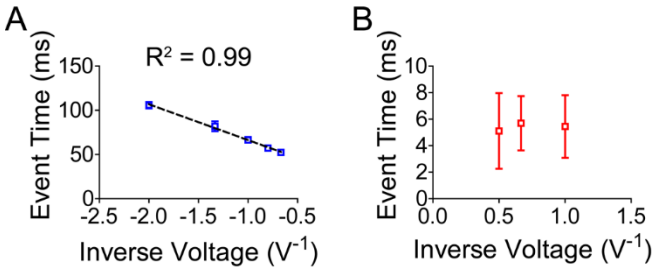

Figure 6.5. Duration of the ion current pulses as a function of inverse voltage measured in (A) 100 mM $LiCO_4$ (water), and (B) 200 mM $LiClO_4$ (propylene carbonate). Recordings in panel (A) were performed with the same 860 nm pore as shown in Figure 3. Recordings in panel (B) were with the same 1 μm pore as in Figure 6.4.

Figure 6.5 B shows the data set of the event duration time plotted as a function of the inverse voltage in propylene carbonate. The first striking difference between the results in water and propylene carbonate is the independence of the event duration time on voltage in the organic solvent. Note that the uncertainty of determination the passage time is ~2 ms. Since the event duration time on average is only ~5 ms, the ~2 ms uncertainty of each measurement prevents us from verifying whether there is a relationship between the passage time and voltage. The measurement of the event duration could not be

improved by increasing the bandwidth of our recordings[140,141] because this would lead to a significant decrease of the signal-to-noise ratio, and in turn make detecting the events (~100 pA in magnitude) more difficult. Equally unexpected is the event duration time, which is ~10 times shorter than in water for the same voltage, even though the viscosity of propylene carbonate is ~3 times higher than the viscosity of water.[142] The electroosmotic velocity of the particles in 200 mM $LiClO_4$ in propylene carbonate reached 10^{-3} m/s. To confirm these findings, similar recordings were performed with the independently prepared pore whose opening diameter was 780 nm. Ion current pulses with duration times less than 10 ms were again observed using the 200 mM $LiClO_4$ propylene carbonate solution and 400 nm polystyrene particles, further validating the enhancement of the electroosmotic velocity.

The voltage independence of the event duration time prevents us from directly calculating the zeta potential of the PET pore walls in propylene carbonate using eq. (6.5). However, if we assumed that the increased electroosmotic velocity in propylene carbonate was due to the increased ζ_{Pore}, the estimated zeta potential would be ~120 mV once the solvent viscosity was accounted for. Therefore, the magnitude of the positive ζ_{Pore} in propylene carbonate is ~30 times larger than the negative ζ_{Pore} in water. The clear lack of dependence of ζ_{Pore} in propylene carbonate on voltage, at least in the voltage range that we probed, also points to a significantly enhanced zeta potential in this solvent.

The zeta potential allows us to estimate the electrokinetic surface charge density (σ_{el}) which can be considered the charge density at the shear plane with ζ_{Pore}.[38] We can use the Graham equation, which relates the surface potential, ζ_{Pore} in this case, to σ_{el}:[143]

$$\sigma_{el} = \sqrt{8 c_0 \varepsilon_0 \varepsilon_r k_B N_A T}\ sinh\left(\frac{ze\zeta_{Pore}}{2k_B T}\right) \qquad \text{eq. (6.6)}$$

where: c_0 is the bulk salt concentration, k_B the Boltzmann constant, T is the temperature and N_A, the Avogadro number.

Using eq. (6.6), σ_{el} was determined to be equal to ~-3 mC/m^2 in 100 mM aqueous $LiClO_4$ and ~+0.3 C/m^2 in 200 mM $LiClO_4$ in propylene carbonate. To further understand the estimated value of σ_{el}, we need to consider the origin of the surface potential in these two solvent systems. A PET pore in contact with an aqueous solvent will be negatively

charged due to the presence of the dissociated, surface carboxyl groups. The density of carboxyl groups is known to be ~1 per nm^2. However, the shear plane is located in the solution beyond the outer Helmholtz layer.[38] Consequently, due to the charge screening, ζ_{Pore} in high ionic strength solutions is significantly lower than the potential right at the surface. Propylene carbonate is a polar, aprotic solvent. Therefore, it is not expected to participate in any Brønsted-Lowry acid-base reactions with the surface carboxyl groups of the PET pore walls and change its surface potential. The positive surface charge in propylene carbonate was postulated to have originated from the adsorption of Li^+ ions and possible ordering of solvent molecules at the interface.[25,41] Since the location and density of the adsorbed Li^+ ions are not limited by the specific chemical groups on the polymer surface, it is possible that the surface charge from the adsorbed Li^+ ions is screened differently than what is predicted by the (classical) Poisson-Boltzmann equation. The estimated σ_{el} of +0.3 C/m^2 corresponds to ~2 Li^+ ions per nm^2. Admittedly, we do not have an explanation for the large magnitude of zeta potential and electrokinetic charge density in propylene carbonate. However, we anticipate that future modeling will be able to unravel the atomistic structure of this and other organic solid-liquid interfaces.

Chapter 7
Conclusions and Future Directions

Throughout this dissertation, a variety of analytical techniques have been investigated and developed to address and deepen our understanding of the underlying mechanisms that govern ionic transport. Though fundamental in nature, the goal for much of this research has been to develop new low detection limit, chemical sensing platforms, and separation (desalination) systems. Achieving these goals has required the design and implementation of elegant experimentation in which PET meso- and nano- pores of varying diameters, shapes, and geometries are used as model systems to probe the electrochemical properties of solid-liquid interfaces in aqueous and organic media. The research presented in this doctoral work represents a continued application of PET pores, expanding and improving on the chemical resolution of the researched phenomena to date.[76,144]

Current-voltage curves recorded with single, conically shaped nanopores in the presence of bulky, chromium, trivalent (Cr^{3+}) cations and sulfate (SO_4^{2-}) anions, revealed that once the small tip opening reached a diameter of 10 nm, the pore began exhibiting ion current fluctuations in time and negative incremental resistance(s) (Chapter 5). Our measurements revealed that the pores become partially sterically occluded with the bulky ions in nanopores with opening diameters less than 5 nm.

Additionally, current-voltage curves obtained in a salt concentration gradient afforded information on the direction of electroosmotic flow in water and propylene carbonate This together with the electroosmotic translocation of uncharged polystyrene particles informed us not only about the polarity of the surface potential but also, the magnitude of the zeta potential of the PET pore walls in propylene carbonate (Chapter 6). The magnitude of the pore walls positive zeta potential in propylene carbonate was shown to be significantly greater than the magnitude of the negative zeta potential in water.[39]

To expand the technical diversity and precision of quantifying the zeta potential of the PET pore walls in propylene carbonate, preliminary streaming current measurements, and dynamic light scattering measurements of silica particles in acetonitrile were also

used to systematically study the solid-liquid interface. These experiments are currently being implemented and in addition to the work above, further illustrate how ubiquitous this phenomenon is.

The studies presented here and going forward will hopefully be complimented by the gleaning of information about the solid-liquid interface and used as a basis to further develop, explore better techniques, methodologies, and numerical models to investigate ionic transport at the nanoscale.

References

(1) Sine, S. M. End-Plate Acetylcholine Receptor: Structure, Mechanism, Pharmacology, and Disease. *Physiol. Rev.* **2012**, *92* (3), 1189–1234. https://doi.org/10.1152/physrev.00015.2011.

(2) Ito, K.; Dulon, D. Nonselective Cation Conductance Activated by Muscarinic and Purinergic Receptors in Rat Spiral Ganglion Neurons. *Am. J. Physiol. - Cell Physiol.* **2002**, *282* (5 51-5), 1121–1135. https://doi.org/10.1152/ajpcell.00364.2001.

(3) Adam Moser, Kevin Range, and D. M. Y. END-PLATE ACETYLCHOLINE RECEPTOR: STRUCTURE, MECHANISM,. *Bone* **2008**, *23* (1), 1–7. https://doi.org/10.1038/jid.2014.371.

(4) Yu, F. H.; Catterall, W. A. The VGL-Chanome: A Protein Superfamily Specialized for Electrical Signaling and Ionic Homeostasis. *Science's STKE : signal transduction knowledge environment*. 2004, pp 1–18. https://doi.org/10.1126/stke.2532004re15.

(5) Jiang, Y.; Lee, A.; Chen, J.; Cadene, M.; Chait, B. T.; MacKinnon, R. The Open Pore Conformation of Potassium Channels. *Nature* **2002**, *417* (6888), 523–526. https://doi.org/10.1038/417523a.

(6) Nieoullon, A. Dopamine and the Regulation of Cognition and Attention. **2002**, *67* (November 2001), 53–83.

(7) Ballard, C.; Gauthier, S.; Corbett, A.; Brayne, C.; Aarsland, D.; Jones, E. Alzheimer's Disease. *Lancet* **2011**, *377* (9770), 1019–1031. https://doi.org/10.1016/S0140-6736(10)61349-9.

(8) Palmer, A. M. Neuroprotective Therapeutics for Alzheimers Disease: Progress and Prospects. *Trends Pharmacol. Sci.* **2011**, *32* (3), 141–147. https://doi.org/10.1016/j.tips.2010.12.007.

(9) Guo, Q.; Sopher, B. L.; Furukawa, K.; Pham, D. G.; Robinson, N.; Martin, G. M.;

Mattson, M. P. Alzheimer's Presenilin Mutation Sensitizes Neural Cells to Apoptosis Induced by Trophic Factor Withdrawal and Amyloid β-Peptide: Involvement of Calcium and Oxyradicals. *J. Neurosci.* **1997**, *17* (11), 4212–4222. https://doi.org/10.1523/jneurosci.17-11-04212.1997.

(10) Shulman, J. M.; De Jager, P. L.; Feany, M. B. Parkinson's Disease: Genetics and Pathogenesis. *Annu. Rev. Pathol. Mech. Dis.* **2011**, *6*, 193–222. https://doi.org/10.1146/annurev-pathol-011110-130242.

(11) Powell, M. R.; Sullivan, M.; Vlassiouk, I.; Constantin, D.; Sudre, O.; Martens, C. C.; Eisenberg, R. S.; Siwy, Z. S. Nanoprecipitation-Assisted Ion Current Oscillations. *Nat. Nanotechnol.* **2008**, *3* (1), 51–57. https://doi.org/10.1038/nnano.2007.420.

(12) He, Y.; Gillespie, D.; Boda, D.; Vlassiouk, I.; Eisenberg, R. S.; Siwy, Z. S. Tuning Transport Properties of Nanofluidic Devices with Local Charge Inversion. *J. Am. Chem. Soc.* **2009**, *131* (14), 5194–5202. https://doi.org/10.1021/ja808717u.

(13) Davenport, M.; Rodriguez, A.; Shea, K. J.; Siwy, Z. S. Squeezing Ionic Liquids through Nanopores. *Nano Lett.* **2009**, *9* (5), 2125–2128. https://doi.org/10.1021/nl900630z.

(14) Innes, L.; Powell, M. R.; Vlassiouk, I.; Martens, C.; Siwy, Z. S. Precipitation-Induced Voltage-Dependent Ion Current Fluctuations in Conical Nanopores. *J. Phys. Chem. C* **2010**, *114* (18), 8126–8134. https://doi.org/10.1021/jp910815p.

(15) Nguyen, G.; Vlassiouk, I.; Siwy, Z. S. Comparison of Bipolar and Unipolar Ionic Diodes. *Nanotechnology* **2010**, *21* (26). https://doi.org/10.1088/0957-4484/21/26/265301.

(16) Solutions, N.; Bush, S. N.; Ken, J. S.; Martin, C. R. The Ionic Composition and Chemistry Of. **2022**. https://doi.org/10.1021/acsnano.2c02597.

(17) Jiali Li; Derek Stein; Ciaran McMullan; Daniel Branton; Michael J. Aziz; Jene A. Golovchenko. Ion-Beam Sculpting at Nanometre Scales. *Nature* **2001**, *412* (July), 166–169.

(18) Stein, D.; Li, J.; Golovchenko, J. A. Ion-Beam Sculpting Time Scales. *Phys. Rev. Lett.* **2002**, *89* (27), 2–5. https://doi.org/10.1103/PhysRevLett.89.276106.

(19) Storm, A. J.; Chen, J. H.; Ling, X. S.; Zandbergen, H. W.; Dekker, C. Fabrication of Solid-State Nanopores with Single-Nanometre Precision. *Nat. Mater.* **2003**, *2* (8), 537–540. https://doi.org/10.1038/nmat941.

(20) Vlassiouk, I.; Apel, P. Y.; Dmitriev, S. N.; Healy, K.; Siwy, Z. S. Versatile Ultrathin Nanoporous Silicon Nitride Membranes. *Proc. Natl. Acad. Sci. U. S. A.* **2009**, *106* (50), 21039–21044. https://doi.org/10.1073/pnas.0911450106.

(21) Umehara, S.; Pourmand, N.; Webb, C. D.; Davis, R. W.; Yasuda, K.; Karhanek, M. Current Rectification with Poly-L-Lysine-Coated Quartz Nanopipettes. *Nano Lett.* **2006**, *6* (11), 2486–2492. https://doi.org/10.1021/nl061681k.

(22) Karhanek, M.; Kemp, J. T.; Pourmand, N.; Davis, R. W.; Webb, C. D. Single DNA Molecule Detection Using Nanopipettes and Nanoparticles. *Nano Lett.* **2005**, *5* (2), 403–407. https://doi.org/10.1021/nl0480464.

(23) Piper, J. D.; Clarke, R. W.; Korchev, Y. E.; Ying, L.; Klenerman, D. A Renewable Nanosensor Based on a Glass Nanopipette. *J. Am. Chem. Soc.* **2006**, *128* (51), 16462–16463. https://doi.org/10.1021/ja0650899.

(24) Bruckbauer, A.; Ying, L.; Rothery, A. M.; Zhou, D.; Shevchuk, A. I.; Abell, C.; Korchev, Y. E.; Klenerman, D. Writing with DNA and Protein Using a Nanopipet for Controlled Delivery. *J. Am. Chem. Soc.* **2002**, *124* (30), 8810–8811. https://doi.org/10.1021/ja026816c.

(25) Plett, T.; Shi, W.; Zeng, Y.; Mann, W.; Vlassiouk, I.; Baker, L. A.; Siwy, Z. S. Rectification of Nanopores in Aprotic Solvents-Transport Properties of Nanopores with Surface Dipoles. *Nanoscale* **2015**, *7* (45), 19080–19091. https://doi.org/10.1039/c5nr06340j.

(26) Mao, P.; Han, J. Fabrication and Characterization of 20 Nm Planar Nanofluidic Channels by Glass-Glass and Glass-Silicon Bonding. *Lab Chip* **2005**, *5* (8), 837–844. https://doi.org/10.1039/b502809d.

(27) Duan, C.; Majumdar, A. Anomalous Ion Transport in 2-Nm Hydrophilic Nanochannels. *Nat. Nanotechnol.* **2010**, *5* (12), 848–852. https://doi.org/10.1038/nnano.2010.233.

(28) Tunuguntla, R. H.; Zhang, Y.; Henley, R. Y.; Yao, Y. C.; Pham, T. A.; Wanunu, M.; Noy, A. Response to Comment on “Enhanced Water Permeability and Tunable Ion Selectivity in Subnanometer Carbon Nanotube Porins.” *Science (80-.).* **2018**, *359* (6383), 792–796. https://doi.org/10.1126/science.aaq1241.

(29) Li, Y.; Li, Z.; Aydin, F.; Quan, J.; Chen, X.; Yao, Y. C.; Zhan, C.; Chen, Y.; Pham, T. A.; Noy, A. Water-Ion Permselectivity of Narrow-Diameter Carbon Nanotubes. *Sci. Adv.* **2020**, *6* (38). https://doi.org/10.1126/sciadv.aba9966.

(30) Ma, T.; Janot, J. M.; Balme, S. Track-Etched Nanopore/Membrane: From Fundamental to Applications. *Small Methods* **2020**, *4* (9). https://doi.org/10.1002/smtd.202000366.

(31) Zhang, Z.; Wen, L.; Jiang, L. Bioinspired Smart Asymmetric Nanochannel Membranes. *Chem. Soc. Rev.* **2018**, *47* (2), 322–356. https://doi.org/10.1039/c7cs00688h.

(32) Hou, X.; Guo, W.; Jiang, L. Biomimetic Smart Nanopores and Nanochannels. *Chem. Soc. Rev.* **2011**, *40* (5), 2385–2401. https://doi.org/10.1039/c0cs00053a.

(33) Siwy, Z. S.; Howorka, S. Engineered Voltage-Responsive Nanopores. *Chem. Soc. Rev.* **2010**, *39* (3), 1115–1132. https://doi.org/10.1039/b909105j.

(34) Epsztein, R.; DuChanois, R. M.; Ritt, C. L.; Noy, A.; Elimelech, M. Towards Single-Species Selectivity of Membranes with Subnanometre Pores. *Nat. Nanotechnol.* **2020**, *15* (6), 426–436. https://doi.org/10.1038/s41565-020-0713-6.

(35) Stein, D.; Kruithof, M.; Dekker, C. Surface-Charge-Governed Ion Transport in Nanofluidic Channels. *Phys. Rev. Lett.* **2004**, *93* (3), 1–4. https://doi.org/10.1103/PhysRevLett.93.035901.

(36) Daiguji, H. Ion Transport in Nanofluidic Channels. *Chem. Soc. Rev.* **2010**, *39* (3), 901–911. https://doi.org/10.1039/b820556f.

(37) Schoch, R. B.; Han, J.; Renaud, P. Transport Phenomena in Nanofluidics. *Reviews of Modern Physics*. 2008, pp 839–883. https://doi.org/10.1103/RevModPhys.80.839.

(38) Delgado, A. V.; González-Caballero, F.; Hunter, R. J.; Koopal, L. K.; Lyklema, J. Measurement and Interpretation of Electrokinetic Phenomena. *J. Colloid Interface Sci.* **2007**, *309* (2), 194–224. https://doi.org/10.1016/j.jcis.2006.12.075.

(39) Russell, W. S.; Siwy, Z. Enhanced Electro-Osmosis in Propylene Carbonate Salt Solutions. *J. Chem. Phys.* **2021**, *154* (13), 1–9. https://doi.org/10.1063/5.0044402.

(40) Ali, M.; Yameen, B.; Cervera, J.; Ramírez, P.; Neumann, R.; Ensinger, W.; Knoll, W.; Azzaroni, O. Layer-by-Layer Assembly of Polyelectrolytes into Ionic Current Rectifying Solid-State Nanopores: Insights from Theory and Experiment. *J. Am. Chem. Soc.* **2010**, *132* (24), 8338–8348. https://doi.org/10.1021/ja101014y.

(41) Lucas, R. A.; Lin, C.-Y.; Siwy, Z. S. Electrokinetic Phenomena in Organic Solvents. *J. Phys. Chem. B* **2019**, *123* (28), 6123–6131. https://doi.org/10.1021/acs.jpcb.9b04969.

(42) Kohli, P.; Harrell, C. C.; Cao, Z.; Gasparac, R.; Tan, W.; Martin, C. R. DNA-Functionalized Nanotube, Membranes with Single-Base Mismatch Selectivity. *Science (80-.).* **2004**, *305* (5686), 984–986. https://doi.org/10.1126/science.1100024.

(43) Acar, E. T.; Buchsbaum, S. F.; Combs, C.; Fornasiero, F.; Siwy, Z. S. Biomimetic Potassium-Selective Nanopores. **2019**, No. February, 1–8.

(44) Vlassiouk, I.; Siwy, Z. S. Nanofluidic Diode. *Nano Lett.* **2007**, *7* (3), 552–556. https://doi.org/10.1021/nl062924b.

(45) Ali, M.; Nasir, S.; Ensinger, W. Bioconjugation-Induced Ionic Current Rectification in Aptamer-Modified Single Cylindrical Nanopores. *Chem. Commun.* **2015**, *51* (16), 3454–3457. https://doi.org/10.1039/c5cc00257e.

(46) Sparreboom, W.; Van Den Berg, A.; Eijkel, J. C. T. Principles and Applications of Nanofluidic Transport. *Nat. Nanotechnol.* **2009**, *4* (11), 713–720.

https://doi.org/10.1038/nnano.2009.332.

(47) Innes, L.; Gutierrez, D.; Mann, W.; Buchsbaum, S. F.; Siwy, Z. S. Presence of Electrolyte Promotes Wetting and Hydrophobic Gating in Nanopores with Residual Surface Charges. *Analyst* **2015**, *140* (14), 4804–4812. https://doi.org/10.1039/c4an02244k.

(48) Vlassiouk, I.; Smimov, S.; Siwy, Z. Nanofluidic Ionic Diodes. Comparison of Analytical and Numerical Solutions. *ACS Nano* **2008**, *2* (8), 1589–1602. https://doi.org/10.1021/nn800306u.

(49) Apel, P. Y.; Korchev, Y. E.; Siwy, Z.; Spohr, R.; Yoshida, M. Diode-like Single-Ion Track Membrane Prepared by Electro-Stopping. *Nucl. Instruments Methods Phys. Res. Sect. B Beam Interact. with Mater. Atoms* **2001**, *184* (3), 337–346. https://doi.org/10.1016/S0168-583X(01)00722-4.

(50) Karnik, R.; Duan, C.; Castelino, K.; Daiguji, H.; Majumdar, A. Rectification of Ionic Current in a Nanofluidic Diode. *Nano Lett.* **2007**, *7* (3), 547–551. https://doi.org/10.1021/nl062806o.

(51) Fan, R.; Yue, M.; Karnik, R.; Majumdar, A.; Yang, P. Polarity Switching and Transient Responses in Single Nanotube Nanofluidic Transistors. *Phys. Rev. Lett.* **2005**, *95* (8), 1–4. https://doi.org/10.1103/PhysRevLett.95.086607.

(52) Lucas, R. A.; Siwy, Z. S. Tunable Nanopore Arrays as the Basis for Ionic Circuits. *ACS Appl. Mater. Interfaces* **2020**, *12* (50), 56622–56631. https://doi.org/10.1021/acsami.0c18574.

(53) Weit, C.; Bard, A. J.; Feldberg, S. W. Current Rectification at Quartz Nanopipet Electrodes. *Anal. Chem.* **1997**, *69* (22), 4627–4633. https://doi.org/10.1021/ac970551g.

(54) White, H. S.; Bund, A. Ion Current Rectification at Nanopores in Glass Membranes. *Langmuir* **2008**, *24* (5), 2212–2218. https://doi.org/10.1021/la702955k.

(55) Sexton, L. T.; Horne, L. P.; Martin, C. R. Developing Synthetic Conical Nanopores

for Biosensing Applications. *Mol. Biosyst.* **2007**, *3* (10), 667–685. https://doi.org/10.1039/b708725j.

(56) Vlassiouk, I.; Kozel, T. R.; Siwy, Z. S. Biosensing with Nanofluidic Diodes. *J. Am. Chem. Soc.* **2009**, *131* (23), 8211–8220. https://doi.org/10.1021/ja901120f.

(57) Kasianowicz, J. J. Nanometer-Scale Pores : Potential Applications for Analyte Detection and DNA Characterization. **2002**, *18*, 185–191.

(58) Division, B.; Biology, C.; Cruz, S. Characterization of Individual Polynucleotide Molecules Using a Membrane Channel. **1996**, *93* (November), 13770–13773. https://doi.org/10.1073/pnas.93.24.13770.

(59) Akeson, M.; Branton, D.; Kasianowicz, J. J.; Brandin, E.; Deamer, D. W. Microsecond Time-Scale Discrimination Among Polycytidylic Acid , Polyadenylic Acid , and Polyuridylic Acid as Homopolymers or as Segments Within Single RNA Molecules. *Biophys. J.* **2000**, *77* (6), 3227–3233. https://doi.org/10.1016/S0006-3495(99)77153-5.

(60) Meller, A.; Nivon, L.; Brandin, E.; Golovchenko, J.; Branton, D. Rapid Nanopore Discrimination between Single Polynucleotide Molecules. **2000**, *97* (3), 1079–1084. https://doi.org/10.1073/pnas.97.3.1079.

(61) Li, J.; Gershow, M.; Stein, D.; Brandin, E.; Golovchenko, J. A. DNA Molecules and Configurations in a Solid- State Nanopore Microscope. **2003**, *2* (September), 611–615. https://doi.org/10.1038/nmat965.

(62) Nanopore, S.; Storm, A. J.; Storm, C.; Chen, J.; Zandbergen, H. Fast DNA Translocation through A. **2005**, 1–5.

(63) Hegelbach, N. G.; Rooij, N. F. De; Staufer, U. Sensing Protein Molecules Using Nanofabricated Pores Sensing Protein Molecules Using Nanofabricated Pores. **2019**, *093901* (August 2005), 28–31. https://doi.org/10.1063/1.2180868.

(64) Mara, A.; Siwy, Z.; Trautmann, C.; Wan, J.; Kamme, F. An Asymmetric Polymer Nanopore for Single Molecule Detection. **2004**.

(65) Harrell, C. C.; Choi, Y.; Horne, L. P.; Baker, L. A.; Siwy, Z. S.; Martin, C. R.; Gaines, V.; May, R. V; Final, I.; July, F. Resistive-Pulse DNA Detection with a Conical Nanopore Sensor †. **2006**, No. 31, 10837–10843.

(66) Bayley, H.; Cremer, P. S. Stochastic Sensors Inspired by Biology. **2001**, *413* (September).

(67) Heng, J. B.; Ho, C.; Kim, T.; Timp, R.; Aksimentiev, A.; Grinkova, Y. V; Sligar, S.; Schulten, K.; Timp, G. Sizing DNA Using a Nanometer-Diameter Pore. *Biophys. J.* **2004**, *87* (4), 2905–2911. https://doi.org/10.1529/biophysj.104.041814.

(68) Tian, Y.; Wen, L.; Hou, X.; Hou, G.; Jiang, L. Bioinspired Ion-Transport Properties of Solid-State Single Nanochannels and Their Applications in Sensing. *ChemPhysChem* **2012**, *13* (10), 2455–2470. https://doi.org/10.1002/cphc.201200057.

(69) Siwy, Z.; Trofin, L.; Kohli, P.; Baker, L. A.; Trautmann, C.; Martin, C. R. Protein Biosensors 'based on Biofunctionalized Conical Gold Nanotubes. *J. Am. Chem. Soc.* **2005**, *127* (14), 5000–5001. https://doi.org/10.1021/ja043910f.

(70) Coulter, W. Means for Counting Particles Suspended in a Fluid. 1953. *U.S. Pat. 2,656,508 (1953).* **1953**, 2. https://doi.org/www.google.com/patents/US2656508.

(71) Henriquez, R. R.; Ito, T.; Sun, L.; Crooks, R. M. The Resurgence of Coulter Counting for Analyzing Nanoscale Objects. *Analyst* **2004**, *129* (6), 478–482. https://doi.org/10.1039/b404251b.

(72) Lan, W. J.; Holden, D. A.; Zhang, B.; White, H. S. Nanoparticle Transport in Conical-Shaped Nanopores. *Anal. Chem.* **2011**, *83* (10), 3840–3847. https://doi.org/10.1021/ac200312n.

(73) Song, Y.; Zhang, J.; Li, D. Microfluidic and Nanofluidic Resistive Pulse Sensing: A Review. *Micromachines*. 2017, pp 1–19. https://doi.org/10.3390/mi8070204.

(74) Duchanois, R. M.; Porter, C. J.; Violet, C.; Verduzco, R.; Elimelech, M. Membrane Materials for Selective Ion Separations at the Water – Energy Nexus. https://doi.org/10.1002/adma.202101312.

(75) Zhang, Y.; Schatz, G. C. Conical Nanopores for Efficient Ion Pumping and Desalination. *J. Phys. Chem. Lett.* **2017**, *8* (13), 2842–2848. https://doi.org/10.1021/acs.jpclett.7b01137.

(76) Berne, B. J.; Fourkas, J. T.; Walker, R. A.; Weeks, J. D. Nitriles at Silica Interfaces Resemble Supported Lipid Bilayers. *Acc. Chem. Res.* **2016**, *49* (9), 1605–1613. https://doi.org/10.1021/acs.accounts.6b00169.

(77) Faucher, S.; Aluru, N.; Bazant, M. Z.; Blankschtein, D.; Brozena, A. H.; Cumings, J.; Pedro De Souza, J.; Elimelech, M.; Epsztein, R.; Fourkas, J. T.; et al. Critical Knowledge Gaps in Mass Transport through Single-Digit Nanopores: A Review and Perspective. *J. Phys. Chem. C* **2019**, *123* (35), 21309–21326. https://doi.org/10.1021/acs.jpcc.9b02178.

(78) Müller, S.; Schötz, C.; Picht, O.; Sigle, W.; Kopold, P.; Rauber, M.; Alber, I.; Neumann, R.; Toimil-Molares, M. E. Electrochemical Synthesis of Bi 1-XSb x Nanowires with Simultaneous Control on Size, Composition, and Surface Roughness. *Cryst. Growth Des.* **2012**, *12* (2), 615–621. https://doi.org/10.1021/cg200685c.

(79) Pevarnik, M.; Healy, K.; Toimil-Molares, M. E.; Morrison, A.; Létant, S. E.; Siwy, Z. S. Polystyrene Particles Reveal Pore Substructure as They Translocate. *ACS Nano* **2012**, *6* (8), 7295–7302. https://doi.org/10.1021/nn302413u.

(80) Qiu, Y.; Hinkle, P.; Yang, C.; Bakker, H. E.; Schiel, M.; Wang, H.; Melnikov, D.; Gracheva, M.; Toimil-molares, M. E.; Imhof, A.; et al. Pores with Longitudinal Irregularities Distinguish Objects by Shape. *ACS Nano* **2015**, *9* (4), 4390–4397. https://doi.org/10.1021/acsnano.5b00877.

(81) Qiu, Y.; Lucas, R. A.; Siwy, Z. S. Viscosity and Conductivity Tunable Diode-like Behavior for Meso- and Micropores. *J. Phys. Chem. Lett.* **2017**, *8* (16), 3846–3852. https://doi.org/10.1021/acs.jpclett.7b01804.

(82) Chen, Q.; Liu, Z. Fabrication and Applications of Solid-State Nanopores. *Sensors (Switzerland)* **2019**, *19* (8). https://doi.org/10.3390/s19081886.

(83) Adla, A.; Fuess, H.; Trautmann, C. Characterization of Heavy Ion Tracks in Polymers by Transmission Electron Microscopy. *J. Polym. Sci. Part B Polym. Phys.* **2003**, *41* (22), 2892–2901. https://doi.org/10.1002/polb.10614.

(84) DeSorbo, W. Ultraviolet Effects and Aging Effects on Etching Characteristics of Fission Tracks in Polycarbonate Film. *Nucl. Tracks* **1979**, *3* (1–2), 13–32. https://doi.org/10.1016/0191-278X(79)90026-X.

(85) Zhu, Z.; Maekawa, Y.; Liu, Q.; Yoshida, M. Influence of UV Light Illumination on Latent Track Structure in PET. *Nucl. Instruments Methods Phys. Res. Sect. B Beam Interact. with Mater. Atoms* **2005**, *236* (1–4), 61–67. https://doi.org/10.1016/j.nimb.2005.03.251.

(86) Bard, A. J.; Faulkner, L. R.; York, N.; @bullet, C.; Brisbane, W.; Toronto, S. E. *ELECTROCHEMICAL METHODS Fundamentals and Applications*; 1944. https://doi.org/10.1016/B978-0-12-381373-2.00056-9.

(87) Romano, J. D.; Price, R. H. The Conical Resistor Conundrum: A Potential Solution. *Am. J. Phys.* **1996**, *64* (9), 1150–1153. https://doi.org/10.1119/1.18335.

(88) Wharton, J. E.; Jin, P.; Sexton, L. T.; Horne, L. P.; Sherrill, S. A.; Mino, W. K.; Martin, C. R. A Method for Reproducibly Preparing Synthetic Nanopores for Resistive-Pulse Biosensors. *Small* **2007**, *3* (8), 1424–1430. https://doi.org/10.1002/smll.200700106.

(89) Ali, M.; Ramirez, P.; Mafé, S.; Neumann, R.; Ensinger, W. A PH-Tunable Nanofluidic Diode with a Broad Range of Rectifying Properties. *ACS Nano* **2009**, *3* (3), 603–608. https://doi.org/10.1021/nn900039f.

(90) Tybrandt, K.; Forchheimer, R.; Berggren, M. Logic Gates Based on Ion Transistors. *Nat. Commun.* **2012**, *3* (May). https://doi.org/10.1038/ncomms1869.

(91) Gabrielsson, E. O.; Tybrandt, K.; Berggren, M. Polyphosphonium-Based Ion Bipolar Junction Transistors. *Biomicrofluidics* **2014**, *8* (6), 9929–9932. https://doi.org/10.1063/1.4902909.

(92) Wolf, A.; Reber, N.; Apel, P. Y.; Fischer, B. E.; Spohr, R. Electrolyte Transport in

Charged Single Ion Track Capillaries. *Nucl. Inst. Methods Phys. Res. B* **1995**, *105* (1–4), 291–293. https://doi.org/10.1016/0168-583X(95)00577-3.

(93) Spohr, R.; Spohr, R. Formation of the Latent Track. *Ion Tracks Microtechnology* **1990**, *51* (1987), 93–125. https://doi.org/10.1007/978-3-322-83103-3_4.

(94) Buchsbaum, S. F.; Nguyen, G.; Howorka, S.; Siwy, Z. S. DNA-Modified Polymer Pores Allow PH- and Voltage-Gated Control of Channel Flux. **2014**, *26* (ii).

(95) Kao, C. Y.; Cheng, W. H.; Wan, B. Z. Investigation of Alkaline Hydrolysis of Polyethylene Terephthalate by Differential Scanning Calorimetry and Thermogravimetric Analysis. *J. Appl. Polym. Sci.* **1998**, *70* (10), 1939–1945. https://doi.org/10.1002/(SICI)1097-4628(19981205)70:10<1939::AID-APP8>3.0.CO;2-G.

(96) Asakuma, Y.; Nakagawa, K.; Maeda, K.; Fukui, K. Theoretical Study of the Transesterification Reaction of Polyethylene Terephthalate under Basic Conditions. *Polym. Degrad. Stab.* **2009**, *94* (2), 240–245. https://doi.org/10.1016/j.polymdegradstab.2008.10.029.

(97) Schoemaker, F. C.; Grobbe, N.; Schakel, M. D.; De Ridder, S. A. L.; Slob, E. C.; Smeulders, D. M. J. Experimental Validation of the Electrokinetic Theory and Development of Seismoelectric Interferometry by Cross-Correlation. *Int. J. Geophys.* **2012**, *2012* (January 2014). https://doi.org/10.1155/2012/514242.

(98) Qiu, Y.; Ma, J.; Chen, Y. Ionic Behavior in Highly Concentrated Aqueous Solutions Nanoconfined between Discretely Charged Silicon Surfaces. *Langmuir* **2016**, *32* (19), 4806–4814. https://doi.org/10.1021/acs.langmuir.6b01149.

(99) Grosberg, A. Y.; Nguyen, T. T.; Shklovskii, B. I. Colloquium: The Physics of Charge Inversion in Chemical and Biological Systems. *Rev. Mod. Phys.* **2002**, *74* (2), 329–345. https://doi.org/10.1103/RevModPhys.74.329.

(100) Van Der Heyden, F. H. J.; Stein, D.; Besteman, K.; Lemay, S. G.; Dekker, C. Charge Inversion at High Ionic Strength Studied by Streaming Currents. *Phys. Rev. Lett.* **2006**, *96* (22), 1–4. https://doi.org/10.1103/PhysRevLett.96.224502.

(101) Li, S. X.; Guan, W.; Weiner, B.; Reed, M. A. Direct Observation of Charge Inversion in Divalent Nanofluidic Devices. *Nano Lett.* **2015**, *15* (8), 5046–5051. https://doi.org/10.1021/acs.nanolett.5b01115.

(102) Besteman, K.; Van Eijk, K.; Lemay, S. G. Charge Inversion Accompanies DNA Condensation by Multivalent Ions. *Nat. Phys.* **2007**, *3* (9), 641–644. https://doi.org/10.1038/nphys697.

(103) Shklovskii, B. I. Screening of a Macroion by Multivalent Ions: Correlation-Induced Inversion of Charge. *Phys. Rev. E - Stat. Physics, Plasmas, Fluids, Relat. Interdiscip. Top.* **1999**, *60* (5), 5802–5811. https://doi.org/10.1103/PhysRevE.60.5802.

(104) Besteman, K.; Zevenbergen, M. A. G.; Lemay, S. G. Charge Inversion by Multivalent Ions: Dependence on Dielectric Constant and Surface-Charge Density. *Phys. Rev. E - Stat. Nonlinear, Soft Matter Phys.* **2005**, *72* (6), 1–9. https://doi.org/10.1103/PhysRevE.72.061501.

(105) Wernersson, E.; Kjellander, R.; Lyklema, J. Charge Inversion and Ion-Ion Correlation Effects at the Mercury/Aqueous MgSO4 Interface: Toward the Solution of a Long-Standing Issue. *J. Phys. Chem. C* **2010**, *114* (4), 1849–1866. https://doi.org/10.1021/jp906759e.

(106) Gurnev, P. A.; Bezrukov, S. M. Inversion of Membrane Surface Charge by Trivalent Cations Probed with a Cation-Selective Channel. *Langmuir* **2012**, *28* (45), 15824–15830. https://doi.org/10.1021/la302676t.

(107) Besteman, K.; Zevenbergen, M. A. G.; Heering, H. A.; Lemay, S. G. Direct Observation of Charge Inversion by Multivalent Ions. **2004**, No. October, 4–7. https://doi.org/10.1103/PhysRevLett.93.170802.

(108) Shklovskii, B. I. Wigner Crystal Model of Counterion Induced Bundle Formation of Rodlike Polyelectrolytes. *Phys. Rev. Lett.* **1999**, *82* (16), 3268–3271. https://doi.org/10.1103/PhysRevLett.82.3268.

(109) Li, H. K.; Pedro De Souza, J.; Zhang, Z.; Martis, J.; Sendgikoski, K.; Cumings, J.;

Bazant, M. Z.; Majumdar, A. Imaging Arrangements of Discrete Ions at Liquid-Solid Interfaces. *Nano Lett.* **2020**. https://doi.org/10.1021/acs.nanolett.0c02669.

(110) Ramirez, P.; Manzanares, J. A.; Cervera, J.; Gomez, V.; Ali, M.; Pause, I.; Ensinger, W.; Mafe, S. Nanopore Charge Inversion and Current-Voltage Curves in Mixtures of Asymmetric Electrolytes. *J. Memb. Sci.* **2018**, *563* (March), 633–642. https://doi.org/10.1016/j.memsci.2018.06.032.

(111) Belaya, M.; Levadny, V.; Pink, D. A. Electric Double Layer near Soft Permeable Interfaces. 1. Local Electrostatic. *Langmuir* **1994**, *10* (6), 2010–2014. https://doi.org/10.1021/la00018a061.

(112) Aguilella-Arzo, M.; Aguilella, V. M.; Eisenberg, R. S. Computing Numerically the Access Resistance of a Pore. *Eur. Biophys. J.* **2005**, *34* (4), 314–322. https://doi.org/10.1007/s00249-004-0452-x.

(113) Hall, J. E. Access Resistance of a Small Circular Pore. *J. Gen. Physiol.* **1975**, *66* (4), 531–532. https://doi.org/10.1085/jgp.66.4.531.

(114) Kosińska, I. D.; Goychuk, I.; Kostur, M.; Schmid, G.; Hänggi, P. Rectification in Synthetic Conical Nanopores: A One-Dimensional Poisson-Nernst-Planck Model. *Phys. Rev. E - Stat. Nonlinear, Soft Matter Phys.* **2008**, *77* (3), 1–10. https://doi.org/10.1103/PhysRevE.77.031131.

(115) Cervera, J.; Schiedt, B.; Neumann, R.; Mafá, S.; Ramírez, P. Ionic Conduction, Rectification, and Selectivity in Single Conical Nanopores. *J. Chem. Phys.* **2006**, *124* (10). https://doi.org/10.1063/1.2179797.

(116) Constantin, D.; Siwy, Z. S. Poisson-Nernst-Planck Model of Ion Current Rectification through a Nanofluidic Diode. *Phys. Rev. E - Stat. Nonlinear, Soft Matter Phys.* **2007**, *76* (4), 1–10. https://doi.org/10.1103/PhysRevE.76.041202.

(117) Harris, D. C. *Quantitative Chemical Analysis*, Eighth Edi.; W. H. Freeman, 2010.

(118) Vlassiouk, I.; Smirnov, S.; Siwyt, Z. Ionic Selectivity of Single Nanochannels. *Nano Lett.* **2008**, *8* (7), 1978–1985. https://doi.org/10.1021/nl800949k.

(119) Petsev, D. N.; Lopez, G. P. Electrostatic Potential and Electroosmotic Flow in a Cylindrical Capillary Filled with Symmetric Electrolyte: Analytic Solutions in Thin Double Layer Approximation. *J. Colloid Interface Sci.* **2006**, *294* (2), 492–498. https://doi.org/10.1016/j.jcis.2005.07.037.

(120) Siwy, Z. S. Ion-Current Rectification in Nanopores and Nanotubes with Broken Symmetry. *Adv. Funct. Mater.* **2006**, *16* (6), 735–746. https://doi.org/10.1002/adfm.200500471.

(121) Guo, W.; Tian, Y.; Jiang, L. Asymmetric Ion Transport through Ion-Channel-Mimetic Solid-State Nanopores. *Acc. Chem. Res.* **2013**, *46* (12), 2834–2846. https://doi.org/10.1021/ar400024p.

(122) Powell, M. R.; Vlassiouk, I.; Martens, C.; Siwy, Z. S. Nonequilibrium 1/f Noise in Rectifying Nanopores. *Phys. Rev. Lett.* **2009**, *103* (24), 9–12. https://doi.org/10.1103/PhysRevLett.103.248104.

(123) Cervera, J.; Schiedt, B.; Neumann, R.; Mafá, S.; Ramírez, P. Ionic Conduction, Rectification, and Selectivity in Single Conical Nanopores. *J. Chem. Phys.* **2006**, *124* (10). https://doi.org/10.1063/1.2179797.

(124) Ali, M.; Ramirez, P.; Nasir, S.; Cervera, J.; Mafe, S.; Ensinger, W. Ionic Circuitry with Nanofluidic Diodes. *Soft Matter* **2019**, *15* (47), 9682–9689. https://doi.org/10.1039/c9sm01654f.

(125) Yameen, B.; Ali, M.; Neumann, R.; Ensinger, W.; Knoll, W.; Azzaroni, O. Single Conical Nanopores Displaying PH-Tunable Rectifying Characteristics. Manipulating Ionic Transport with Zwitterionic Polymer Brushes. *J. Am. Chem. Soc.* **2009**, *131* (6), 2070–2071. https://doi.org/10.1021/ja8086104.

(126) Pietschmann, J. F.; Wolfram, M. T.; Burger, M.; Trautmann, C.; Nguyen, G.; Pevarnik, M.; Bayer, V.; Siwy, Z. Rectification Properties of Conically Shaped Nanopores: Consequences of Miniaturization. *Phys. Chem. Chem. Phys.* **2013**, *15* (39), 16917–16926. https://doi.org/10.1039/c3cp53105h.

(127) Hsu, J. P.; Yang, S. T.; Lin, C. Y.; Tseng, S. Ionic Current Rectification in a

Conical Nanopore: Influences of Electroosmotic Flow and Type of Salt. *J. Phys. Chem. C* **2017**, *121* (8), 4576–4582. https://doi.org/10.1021/acs.jpcc.6b09907.

(128) DeBlois, R. W.; Bean, C. P.; Wesley, R. K. A. Electrokinetic Measurements with Submicron Particles and Pores by the Resistive Pulse Technique. *Journal of Colloid And Interface Science*. 1977, pp 323–335. https://doi.org/10.1016/0021-9797(77)90395-2.

(129) Wanunu, M. Nanopores: A Journey towards DNA Sequencing. *Phys. Life Rev.* **2012**, *9* (2), 125–158. https://doi.org/10.1016/j.plrev.2012.05.010.

(130) Kozak, D.; Anderson, W.; Vogel, R.; Chen, S.; Antaw, F.; Trau, M. Simultaneous Size and ζ-Potential Measurements of Individual Nanoparticles in Dispersion Using Size-Tunable Pore Sensors. *ACS Nano* **2012**, *6* (8), 6990–6997. https://doi.org/10.1021/nn3020322.

(131) Qiu, Y.; Vlassiouk, I.; Chen, Y.; Siwy, Z. S. Direction Dependence of Resistive-Pulse Amplitude in Conically Shaped Mesopores. *Anal. Chem.* **2016**, *88* (9), 4917–4925. https://doi.org/10.1021/acs.analchem.6b00796.

(132) Pevarnik, M.; Healy, K.; Toimil-Molares, M. E.; Morrison, A.; Létant, S. E.; Siwy, Z. S. Polystyrene Particles Reveal Pore Substructure as They Translocate. *ACS Nano* **2012**, *6* (8), 7295–7302. https://doi.org/10.1021/nn302413u.

(133) Balakrishnan, K. R.; Whang, J. C.; Hwang, R.; Hack, J. H.; Godley, L. A.; Sohn, L. L. Node-Pore Sensing Enables Label-Free Surface-Marker Profiling of Single Cells. *Anal. Chem.* **2015**, *87* (5), 2988–2995. https://doi.org/10.1021/ac504613b.

(134) Bayley, H.; Martin, C. R. Resistive-Pulse Sensing - from Microbes to Molecules. *Chem. Rev.* **2000**, *100* (7), 2575–2594. https://doi.org/10.1021/cr980099g.

(135) Luo, L.; German, S. R.; Lan, W. J.; Holden, D. A.; Mega, T. L.; White, H. S. Resistive-Pulse Analysis of Nanoparticles. *Annu. Rev. Anal. Chem.* **2014**, *7*, 513–535. https://doi.org/10.1146/annurev-anchem-071213-020107.

(136) Howorka, S.; Siwy, Z. Nanopore Analytics: Sensing of Single Molecules. *Chem. Soc. Rev.* **2009**, *38* (8), 2360–2384. https://doi.org/10.1039/b813796j.

(137) Qiu, Y.; Siwy, Z. Probing Charges on Solid-Liquid Interfaces with the Resistive-Pulse Technique. *Nanoscale* **2017**, *9* (36), 13527–13537. https://doi.org/10.1039/c7nr03998k.

(138) DeBlois, R. W.; Bean, C. P. Counting and Sizing of Submicron Particles by the Resistive Pulse Technique. *Rev. Sci. Instrum.* **1970**, *41* (7), 909–916. https://doi.org/10.1063/1.1684724.

(139) Fievet, P.; Szymczyk, A.; Labbez, C.; Aoubiza, B.; Simon, C.; Foissy, A.; Pagetti, J. Determining the Zeta Potential of Porous Membranes Using Electrolyte Conductivity inside Pores. *J. Colloid Interface Sci.* **2001**, *235* (2), 383–390. https://doi.org/10.1006/jcis.2000.7331.

(140) Chien, C. C.; Shekar, S.; Niedzwiecki, D. J.; Shepard, K. L.; Drndić, M. Single-Stranded DNA Translocation Recordings through Solid-State Nanopores on Glass Chips at 10 MHz Measurement Bandwidth. *ACS Nano* **2019**, *13* (9), 10545–10554. https://doi.org/10.1021/acsnano.9b04626.

(141) Rosenstein, J. K.; Wanunu, M.; Merchant, C. A.; Drndic, M.; Shepard, K. L. Integrated Nanopore Sensing Platform with Sub-Microsecond Temporal Resolution. *Nat. Methods* **2012**, *9* (5), 487–492. https://doi.org/10.1038/nmeth.1932.

(142) Barthel, J.; Neueder, R.; Roch, H. Density, Relative Permittivity, and Viscosity of Propylene Carbonate+dimethoxyethane Mixtures from 25 °C to 125 °C. *J. Chem. Eng. Data* **2000**, *45* (6), 1007–1011. https://doi.org/10.1021/je000098x.

(143) Jalil, A. H.; Pyell, U. Quantification of Zeta-Potential and Electrokinetic Surface Charge Density for Colloidal Silica Nanoparticles Dependent on Type and Concentration of the Counterion: Probing the Outer Helmholtz Plane. *J. Phys. Chem. C* **2018**, *122* (8), 4437–4453. https://doi.org/10.1021/acs.jpcc.7b12525.

(144) Nguyen, T. T.; Grosberg, A. Y.; Shklovskii, B. I. Macroions in Salty Water with Multivalent Ions: Giant Inversion of Charge. *Phys. Rev. Lett.* **2000**, *85* (7), 1568–1571. https://doi.org/10.1103/PhysRevLett.85.1568.